Quantifying Cross-Shelf Transport in the East Australian Current System: A Budget-Based Approach

NEIL MALAN,[a] MONINYA ROUGHAN,[a] GEOFFREY J. STANLEY,[b] RYAN HOLMES,[c] AND JUNDE LI[a]

[a] *School of Biological, Earth and Environmental Sciences, and Centre for Marine Science and Innovation, University of New South Wales, Sydney, New South Wales, Australia*

[b] *School of Mathematics and Statistics, University of New South Wales, Sydney, New South Wales, Australia*

[c] *School of Mathematics and Statistics, Climate Change Research Centre, and ARC Centre of Excellence for Climate Extremes, University of New South Wales, Sydney, New South Wales, Australia*

(Manuscript received 30 August 2021, in final form 23 June 2022)

ABSTRACT: Cross-shelf transport plays an important role in the heat, salt, and nutrient budgets of the continental shelf. In this study, we quantify cross-shelf volume transport and explore its dynamics within a high-resolution (2.5–6 km) regional ocean model of the East Australian Current (EAC) System, a western boundary current with a high level of mesoscale eddy activity. We find that the largest time-mean cross-shelf flows (>4 Sv per 100 km; 1 Sv ≡ 10^6 m^3 s^{-1}) occur inshore of the coherent western boundary current, between 26° and 30°S, while the strongest time-varying flows occur in the EAC southern extension, poleward of 32°S, associated with mesoscale eddies. Using a novel diagnostic equation derived from the momentum budget we show that the cross-shelf transport is dominated by the baroclinic and geostrophic component of the velocities, as the EAC jet is relatively free to flow over the variable shelfbreak topography. However, topographic interactions are also important and act through the bottom pressure torque term as a secondary driver of cross-shelf transport. The importance of topographic interaction also increases in shallower water inshore of the coherent jet. Downstream of separation, cross-shelf transport is more time-varying and associated with the interaction of mesoscale eddies with the shelf. The identification of the change in nature and drivers of cross-shelf transport in eddy versus jet dominated regimes may be applicable to understanding cross-shelf transport dynamics in other boundary current systems.

SIGNIFICANCE STATEMENT: Cross-shelf transport, i.e., the movement of water from the open ocean on or off the continental shelf, is not reported often as it is difficult to measure and model. We demonstrate a simple but effective method to do this and, using an ocean model, apply it to the East Australian Current System and show what drives it. The results show two distinct regimes, which differ depending on which part of the current system you are in. Our results help to place observations of cross-shelf transport in better context and provide a framework within which to consider the transport of other things such as heat and carbon from the open ocean to the continental shelf.

KEYWORDS: Boundary currents; Coastal flows; Eddies; Topographic effects

1. Introduction

In coastal and shelf systems, alongshore currents generally dominate the three-dimensional flow. However, due to the strong cross-shelf gradients in temperature, salinity, and biological tracers, cross-shelf flows can have a disproportionately large impact on the physical and biological variability of the shelf system despite their relatively small magnitudes (Brink 2016). This disproportionate importance of cross-shelf flows can be amplified in western boundary current systems, such as the East Australian Current (EAC). The EAC is the western boundary current of the South Pacific subtropical gyre and impacts the continental shelf of eastern Australia in two distinct regimes; the EAC jet, a continuous current flowing poleward along the continental shelf between approximately 25° and 32°S, and the EAC southern extension, an eddy-dominated poleward flow which extends from ~32°S to the southern tip of Tasmania (~42°S) (Oke et al. 2019). These contrasting flow regimes (illustrated in Fig. 1) are divided by the EAC separation zone, where the EAC jet leaves the continental shelf. The exact separation latitude varies from as far upstream as 28°S to as far downstream as 38°S, but most often occurs between 31° and 33°S (Cetina-Heredia et al. 2014) and has been linked to mesoscale eddy-shedding events (Mata et al. 2006; Cetina-Heredia et al. 2014).

The difficulty in quantifying, and the possible impact of cross-shelf flows in this type of western boundary system, is amplified due to large cross-shelf velocity (Fig. 1a) and temperature gradients (Fig. 1b), the latter of which can reach up to 0.2°C km^{-1} in the EAC system (Schaeffer et al. 2013). This means that an intrusion of the poleward flowing EAC onto the continental shelf has the potential to carry with it large amounts of heat or other tracers. However, to quantify the cross-shelf flows ultimately responsible for these large cross-shelf tracer transports, one confronts the difficulty of separating

Denotes content that is immediately available upon publication as open access.

Holmes's current affiliation: School of Geosciences, University of Sydney, Sydney, New South Wales, Australia.

Corresponding author: Neil Malan, neilcmalan@gmail.com

DOI: 10.1175/JPO-D-21-0193.1

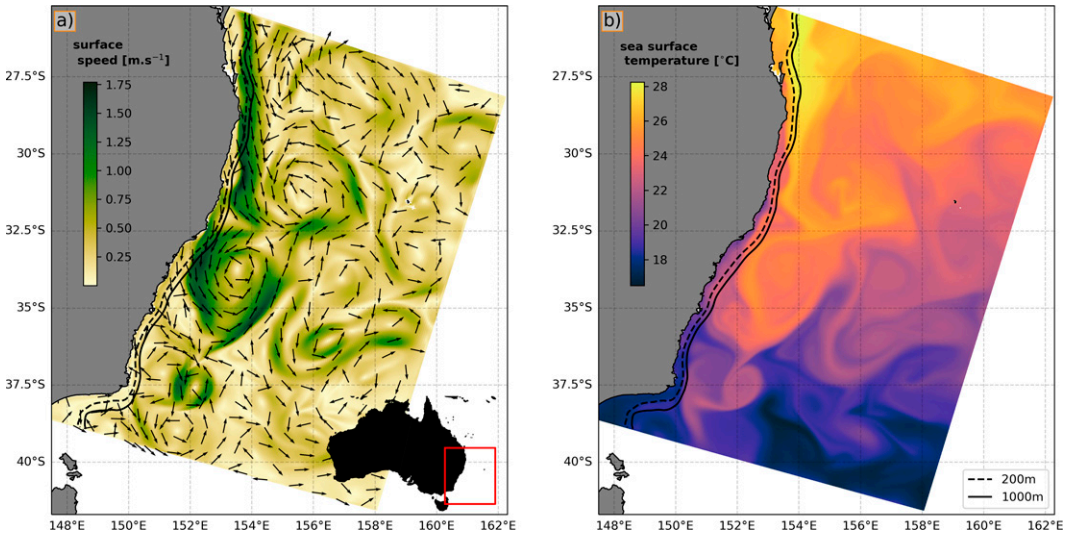

FIG. 1. One day snapshot (12 Jan 1994) from the EAC-ROMS model, showing conditions typical of the EAC system in (a) surface current speed (shaded) and direction (vectors), with the inset map showing the position of the model domain on the Australian coast and (b) sea surface temperature, in the EAC system. The isobaths at 200 m (dashed line) and 1000 m (solid line) are shown in black. Note the relationship between temperature and velocity, the strong along-shelf velocities, as well as the narrow current (jet) equatorward of 32°S and the eddying southern extension poleward of 32°S.

out a small signal (cross-shelf volume transport), from the much larger "noise" of along-shelf volume transport. An accurate understanding of cross-shelf flows and their dynamical drivers is important as, for example, their relative strength is a key determinant of whether a shelf region is a net source or sink of atmospheric carbon (Cai et al. 2006).

The dynamics of cross-shelf mass and tracer transport appear to differ considerably across the different western boundary currents. In the Mid-Atlantic bight on the eastern seaboard of the United States, cross-shore transport of warm Gulf Stream water via warm core rings has been well documented (Cenedese et al. 2013; Zhang and Gawarkiewicz 2015; Zhang and Partida 2018; Cherian and Brink 2018). In the southwest Atlantic, Lagrangian tracking methods in a numerical model show that 95% of shelf water at 32°S was advected onto the shelf far upstream at 22°S and that cross-shelf transport is significantly correlated with local wind stress variability (Combes et al. 2021). In contrast, in the Agulhas Current system, large propagating meanders drive cross-shelf exchange (Malan et al. 2018) and are uncorrelated with local wind variability. In the Kuroshio poleward of Taiwan, the flow is known to intrude onto the shelf as it widens, with the resulting cross-shelf mass transport being attributed to both the Kuroshio jet encountering a steep rise in the bathymetry (Hsueh et al. 1996), as well as large intrusions driven by cyclonic eddies (Vélez-Belchí et al. 2013). Similar dynamics appear to be at play on the Antarctic shelf, with recent work emphasizing the role of bathymetry in the exchange of circumpolar deep water and dense shelf water (Morrison et al. 2020), as well as the role of bottom Ekman transport in driving cross-shelf tracer fluxes (Spence et al. 2017; Webb et al. 2019).

In the EAC system, previous work looking at cross-shelf flows has focused on specific locations upstream and downstream of the EAC separation point using data from mooring arrays (Roughan and Middleton 2002, 2004; Schaeffer et al. 2013) and high-frequency radar systems (Archer et al. 2017). Prior to separation from the coast, the EAC jet itself can act as a barrier to the onshore movement of simulated Lagrangian particles (Roughan et al. 2011). Observational work using moorings at 30° and 34°S has shown that both along- and across-shelf momentum balances are dominated by the barotropic pressure gradient term (Roughan and Middleton 2004; Schaeffer et al. 2013). Similarly to the Antarctic shelf, bottom Ekman transport can also drive cross-shelf tracer transport in the EAC (Roughan and Middleton 2002, 2004). The encroachment of the EAC jet onto the shelf is stronger at 30°S, where the EAC jet is more coherent, compared to downstream of separation at 34°S. Archer et al. (2017) quantify the effect of the EAC jet meandering onto the continental shelf at 30°S, showing a dominant scale of variability at 65–100 days, related to the EAC eddy-shedding time scale.

Other studies have investigated the role of eddy-driven processes as potential drivers of cross-shelf volume transport. Three separate categories have been identified: frontal eddies inshore of the main EAC jet (Schaeffer and Roughan 2017; Mantovanelli et al. 2017; Roughan et al. 2017), mesoscale eddies downstream of the separation point (Cetina-Heredia et al. 2019a,b; Malan et al. 2020; Archer et al. 2020), and the semipermanent cyclonic eddy occurring in the equatorward part of the current, sometimes called the Fraser Gyre (Ribbe and Brieva 2016; Azis Ismail et al. 2017; Azis Ismail and Ribbe 2019). However, the importance of these various processes to cross-shelf mass and tracer transports in the EAC system is currently unknown.

Ribbat et al. (2020) used a limited model domain and 2 years of model output to explore cross-shelf transport at the

EAC separation zone. They used boxes approximately aligned with isobaths to show a maximum in offshore volume transport between 32° and 33°S with variable onshore volume transport from 33° to 34°S. Here we extend and generalize this approach to quantify cross-shelf volume transport, including its variability and dynamical drivers for the first time, along the entire length of the EAC system over two decades.

The paper is laid out as follows. Section 2 introduces the model configuration and a budget-based approach for calculating cross-shelf transport. Section 3 explores the time-mean state and distribution of cross-shelf transport in the EAC system using the budget-based approach. Section 4 derives a new cross-shelf momentum budget and uses it to examine the dynamical drivers of cross-shelf transport. Section 5 looks at eddy and other time-varying effects. Section 6 concludes and summarizes the results and their implications.

2. Model configuration and methods

We use a free-running (i.e., non-data-assimilating) configuration of the Regional Ocean Modeling System (ROMS) that has been used in previous studies of the EAC system (EAC-ROMS) (Kerry et al. 2016; Rocha et al. 2019; Kerry and Roughan 2020; Kerry et al. 2020; Schilling et al. 2020; Phillips et al. 2020; Li et al. 2021b, 2022). The model domain extends from 25.3° to 38.5°S, and from the coast to ~1000 km offshore. The grid is rotated 20° clockwise so as to be aligned with the coastline (Fig. 1). The horizontal resolution is variable in the cross-shelf direction, ranging from 2.5 to 6 km (1/44°–1/18°), with the highest resolution over the continental shelf and 5 km (1/22°) in the along-shelf direction. There are 30 vertical s layers with enhanced vertical resolution in the upper 400 m and the bottom boundary layer. The 2.5-level, second-moment turbulence closure scheme (Mellor and Yamada 1982) is used to parameterize the vertical turbulent mixing of momentum and tracers. Bathymetry is from the 50-m high-resolution Multibeam Dataset for Australia from Geoscience Australia (Whiteway 2009), and horizontal pressure gradient errors are minimized to an acceptable level using careful smoothing to ensure the position of the shelf break is accurate (Kerry et al. 2016). The model initial and boundary conditions are taken from CSIRO's Australia Bluelink ReANalysis (BRAN2016), which has a horizontal resolution of 1/10° (Oke et al. 2008, 2013). The model is forced with the hourly Bureau of Meteorology Atmospheric high-resolution Regional Reanalysis for Australia (BARRA-R) with a horizontal resolution of 12 km (Su et al. 2019). The tidal forcing used in this study is extracted from the TPXO8 global tidal model (Egbert and Erofeeva 2002). The model runs from 1 January 1994 to 1 October 2016, showing a good representation of the hydrodynamics of the shelf waters inshore of the EAC (Li et al. 2021a,b). Model output is saved as daily averages, with momentum diagnostics (used in section 4) output monthly from 2010 to 2015. The higher resolution of the model grid in the cross-shelf direction enables the mesoscale variability, as well as the latitude at which the EAC separates from the coast, to be well represented when compared to satellite altimetry (see Fig. 2 of Kerry et al. 2016). Full details of the model set up, physics parameterizations and validation can be found in Kerry et al. (2016), Kerry and Roughan (2020), and Li et al. (2021a), specifically the EAC separation latitude which is of relevance to this study has been shown to be well represented in this model by Kerry and Roughan (2020).

a. Approaches in quantifying cross-shelf transport

In current systems where along-shelf currents are relatively weak, cross-shelf flow can be estimated by using velocities normal to straight sections angled to approximate the coastline [e.g., Zaba et al. (2020) in the California Current] or if the domain is sufficiently small, on isobaths (Azis Ismail and Ribbe 2019; Ribbat et al. 2020). However, in more typical western boundary current systems, where along-shelf velocities can be more than an order of magnitude greater than cross-shelf velocities, more care is required. Past studies have quantified cross-shelf transport by rotating the model's velocities normal to the local direction of an isobath and then integrating this transport along the length of that isobath (Levin et al. 2019, 2020, 2021; Guerrero et al. 2020). Unless done carefully, the interpolation and rotation operations performed in this process can result in inconsistencies with the mass budget of the underlying numerical model (and may be particularly problematic for high-resolution models which resolve complex bathymetric gradients). To alleviate these issues, we apply a "budget-based" approach which remains true to the numerical discretization of the underlying model (i.e., in this case to the ROMS Arakawa C grid configuration).

We start with the depth-integrated continuity equation

$$-\eta_t = \nabla \cdot \mathbf{U}, \tag{1}$$

where $\mathbf{U} = (U, V) = \int_{-H}^{\eta} \mathbf{u}\, dz$ is the depth-integral of the horizontal velocity vector $\mathbf{u} = (u, v)$ and η_t is the sea surface height tendency. This equation is derived from the Boussinesq continuity equation, integrated over a water column from the seafloor at $z = -H(x, y)$ to the sea surface at $z = \eta(x, y, t)$, and applying the Leibniz integral rule with no-normal flow boundary conditions at the sea floor and kinematic boundary condition at sea surface, and neglecting surface volume fluxes. Here, x and y are the model coordinate directions (i.e., y points 20° east of north, while x points 20° south of east, Fig. 1).

Using the divergence theorem to integrate Eq. (1) over a section of the shelf, bounded by two "zonal" model coordinate surfaces y_1 to the southwest and y_2 to the northeast, the coastline, and the shelf edge (taken as the 1000-m isobath unless otherwise stated) yields

$$-\int\int_A \eta_t\, dA = \int\int_A \nabla \cdot \mathbf{U}\, dA = \int_{x_2(0\text{m})}^{x_2(-1000\text{m})} V(x, y_2) dx - \int_{x_1(0\text{m})}^{x_1(-1000\text{m})} V(x, y_1) dx + \int_{\mathcal{P}} \mathbf{U} \cdot \hat{\mathbf{n}}\, d\ell, \tag{2}$$

where $x_i(h)$ satisfies $-H[x_i(h), y_i] = h$ so that $x_1(0)$, for example, is the x position of the coast at y_1, and $\hat{\mathbf{n}} = \nabla H/|\nabla H|$ is the downslope unit vector. In this study we mainly use the 1000-m isobath as the offshore bound of x, making A the shelf area

between along-coast limits y_1 and y_2 and between the coast and the 1000-m isobath.

In other words, the cross-shelf transport [last term in Eq. (2)] can be simply calculated as the convergence of the "meridional" transport across zonal model coordinate surfaces on the shelf, minus some small influence caused by temporal variations in sea surface height (negligible in this case). This calculation can be applied across the entire shelf, as well as to each individual row of model grid cells extending from the coast to the shelf edge, which we numerically take as the last grid cell in each model row having a bathymetric depth less than 1000 m. Note that this budget-based method does not rely on along-shelf transport being orthogonal to cross-shelf transport, only that the faces of the cells used to calculate the alongshore transport intersect the 1000-m isobath. The method would need to be trivially modified for regions where the isobaths in question are better aligned with the model's U transport component, rather than its V transport component as in our case. The grid of our ROMS configuration is rotated 20° from true north and as this approximates the direction of the shelf edge, for convenience we will refer to transport in the y direction on the model grid as "along-shelf."

A test of the efficacy of this method and its ability to conserve volume is that when integrating the cross-shelf transport calculated from Eq. (2) along the length of the EAC shelf (25.5°–38.9°S), it should balance with the amount of water that flows in and out of the northern and southern boundaries of the EAC shelf. This balance is shown in Fig. 2, with the northern and southern boundaries shown by the gray lines in Fig. 3 at 26° and 38°S, respectively. The residual between the cross-shelf transport, the inflow at the north, and the outflow at the south is negligible (of order 10^{-9} Sv; 1 Sv $\equiv 10^6$ m^3 s^{-1}). It is associated with small influences from 1) the neglect of surface volume fluxes over the shelf and 2) any temporal aliasing in the offline calculation of the SSH tendency term from the time-averaged daily output [left-hand side of Eq. (2)].

3. Along and across-shelf transports in the EAC

Using the budget-based approach we quantify the along-shelf transports and the associated cross-shelf transport across the 1000-m isobath (as summarized in 2° latitude bands in Fig. 3a). All time-mean along-shelf transports are southward (poleward), while cross-shelf transports in the EAC jet region equatorward of 32°S are characterized by large spatially alternating zones of time-mean cross-shelf transport and low variability. In contrast, cross-shelf transports are generally weaker and offshore poleward of 32°S, in the eddy-dominated EAC southern extension. Southward transport on the shelf is 1.89 Sv at 26°S and increases to 5.41 Sv at 28°S, fed by 3.55 Sv of onshore transport in this region. However, a cumulative sum (Fig. 3b) shows that most of this mass leaves the shelf between 28° and 30°S, where there is an offshore cross-shelf transport of 3.34 Sv as the southward transport on the shelf reduces to 2.68 Sv. An increase in southward along-shelf transport to 3.42 Sv at 32°S results in a corresponding onshore transport of 1.12 Sv between 30° and 32°S.

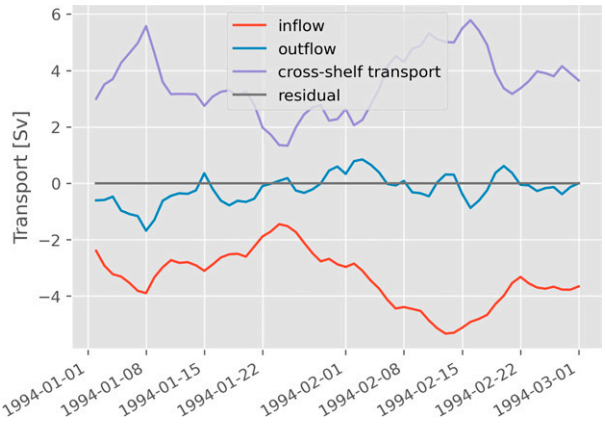

FIG. 2. Time series of the shelf volume budget from Eq. (2) integrated along the length of the EAC-ROMS model domain (25.5°–38.9°S). "Inflow" is the along-shelf transport at the northern end of the model domain, "outflow" is the along-shelf transport at the southern end of the domain (positive values are northward along-shelf transport), "cross-shelf transport" is the line integral of transport across the 1000-m isobath between 25.5° and 38.9°S, with positive values indicating offshore transport, and "residual" is the rate of volume change due to changing sea surface height, which is negligible.

In the more eddy-dominated region poleward of 32°S, the time-mean southward along shelf transport of 1.59 Sv at 34°S is progressively lost offshore, with only 0.02 Sv of southward transport remaining at 38°S. In summary, in the EAC jet region (equatorward of 32°S in Fig. 3b), the southward shelf transport peaks twice (at 28° and 32°S) as a result of net onshore transport, while poleward of 32°S, southward shelf transport decreases with increasing latitude, resulting in net offshore transport. Cross-shelf transport also makes up a greater proportion of the overall shelf circulation (at the scales captured by Fig. 3) in the eddy-dominated region poleward of 32°S than in the EAC jet region. This schematic view is by necessity a simplification to gain a high-level understanding of the nature of the cross and along-shelf volume transport along the length of the EAC system. The cumulative sum of the mean cross-shelf transport (Fig. 3b) shows the complexity of the cross-shelf flows at smaller scales, especially between 28° and 30°S and poleward of 32°S where there are multiple reversals between onshore and offshore transport.

The onshore and offshore transport reversals equatorward of 32°S and thus inshore of the EAC jet appear to be associated with changes in the orientation of the shelf break (see 1000-m isobath in Fig. 3a). Here the jet meanders on and off the shelf [previously studied in observations by Archer et al. (2017)] resulting in high (>0.2 m s^{-1}) time-mean bottom current speeds on the shelf (Fig. 4a). High bottom speed values at 28°, 29°, and 31°S coincide with peaks in onshore time-mean volume transport seen in Fig. 5c. The incursion of the EAC onto the shelf at these points has previously been connected to bottom Ekman upwelling processes using both observational data (Roughan et al. 2003; Roughan and Middleton 2004) and model output (Oke and Middleton 2000),

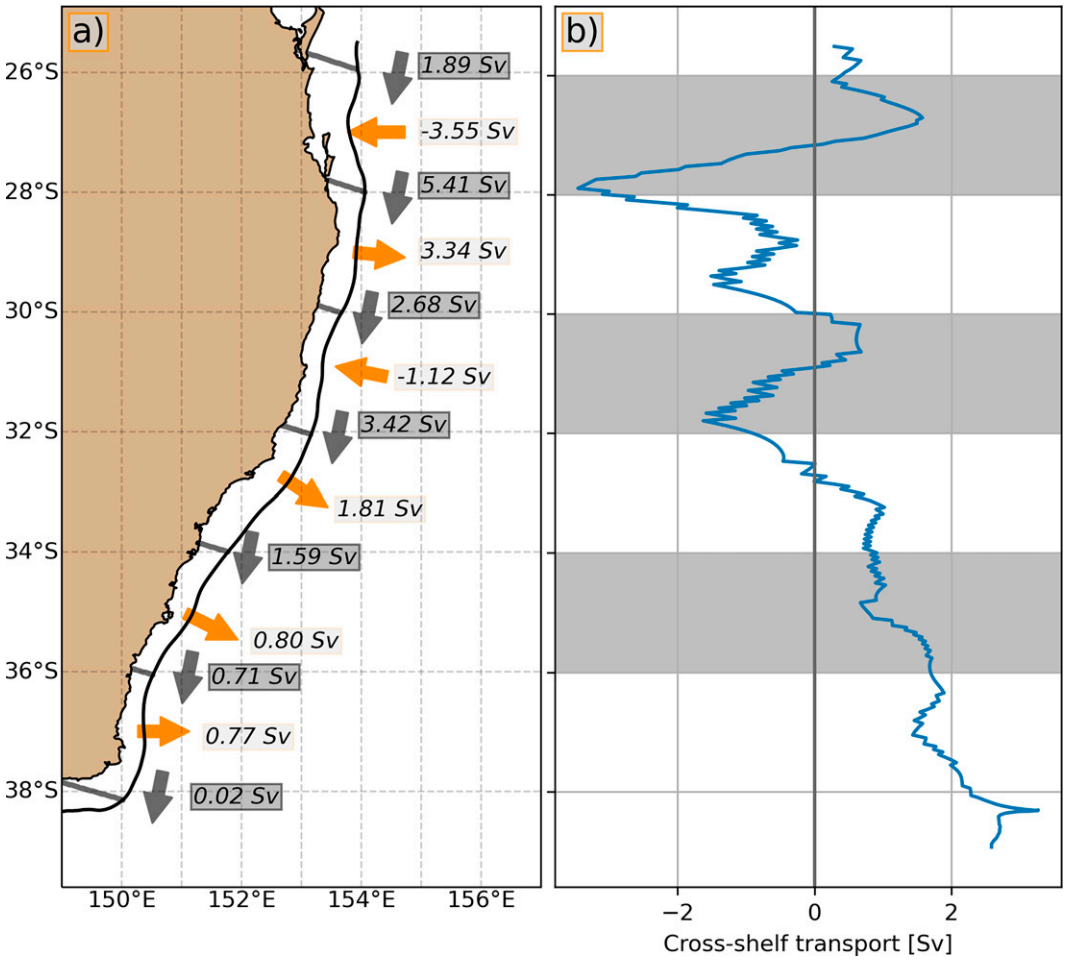

FIG. 3. Schematic view of (a) time-mean along-shelf and across-shelf transports through boxes divided into 2° latitudinal bands that extend from the coast to the 1000-m isobath. Gray arrows show poleward shelf transports (values in dark gray boxes) across sections from the coast to the 1000-m isobath (marked by gray lines), orange lines show cross-shelf transports across 1000-m isobaths at 2° latitudinal intervals (values in light gray boxes). Negative across-shelf values show onshore transport and positive along-shelf values show southward transport and (b) cumulative sum of time-mean 1000-m cross-shelf transport in the EAC system.

and is also connected to an acceleration of the EAC directly downstream of where the shelf narrows and the coastline extends in the form of protruding capes (Cape Byron at 28.6°S and Smoky Cape at 31°S). As was the case for the cross-shelf transport, the time-mean bottom current speed weakens poleward of 32°S while variability increases (Fig. 4b).

The latitudinal distribution of the zones of onshore and offshore cross-shelf transport persists if, instead of transport across the 1000-m isobath, we consider transport across the 200-m isobath (Fig. 6). Although smaller in magnitude due to the shallower water column, the same persistent alternating bands of cross-shelf transport are seen equatorward of 32°S, while the cross-shelf flows poleward of 32°S are far more variable (Fig. 6a). As seen in the 1000-m cross-shelf transport, mean values of cross-shelf transport across the 200-m isobath are highest in the equatorward half of the domain, but with higher standard deviations in the poleward half of the domain (Fig. 6c). The consistency of the cross-shelf flow between the 1000- and 200-m isobaths shows that the drivers of cross-shelf volume transport are likely to be coherent across the shelf break, and not limited specifically to the 1000-m isobath.

4. Diagnosing drivers of time-mean cross-shelf transport

a. Theory

In the previous sections we put forward a simple method for quantifying cross-shelf volume transport, and we described its time-mean state along the latitudinal extent of the EAC system. Next it is useful to look at the dynamical drivers of this time-mean cross-shelf transport in terms of a cross-isobath transport budget derived from the momentum equations.

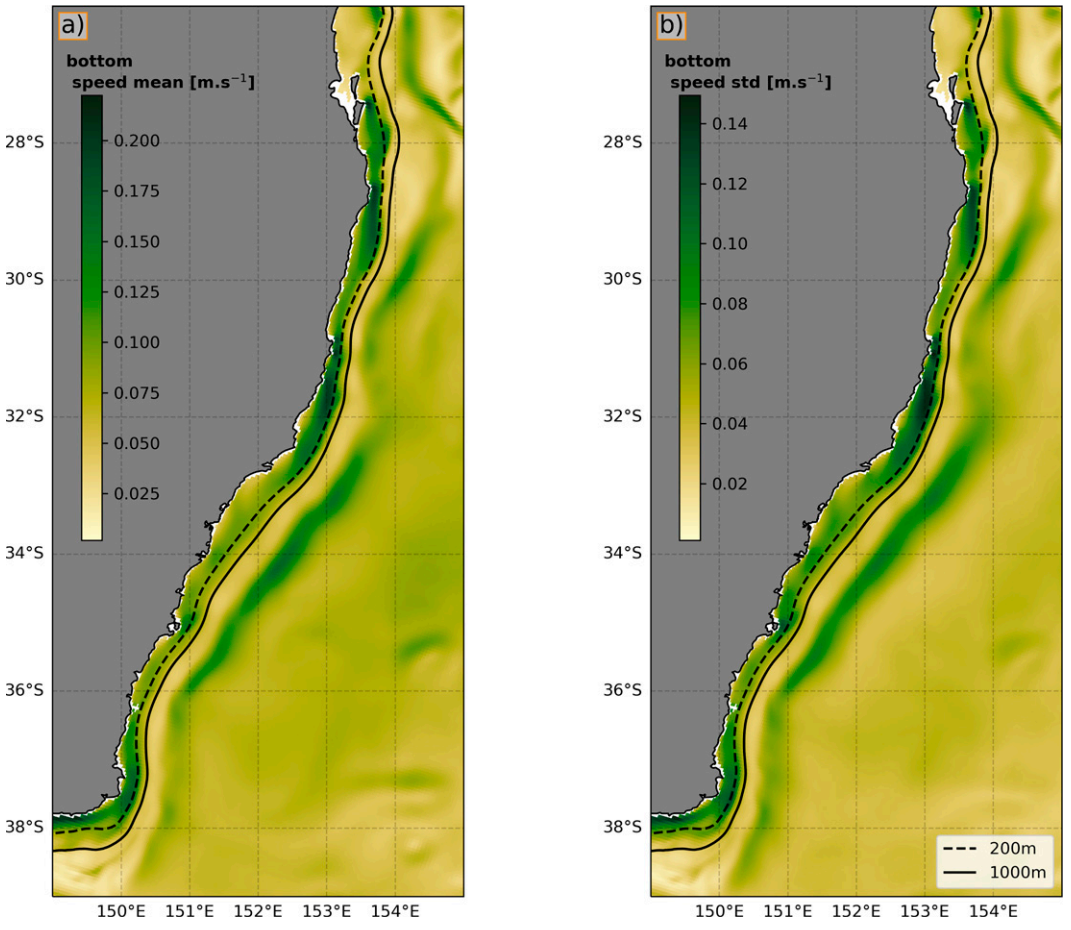

FIG. 4. (a) Time mean and (b) standard deviation of bottom current speed (taken from the deepest model layer) in the EAC system.

To derive a diagnostic formula for the cross-shelf transport, we begin with the instantaneous, primitive, and Boussinesq horizontal momentum equation written as

$$f\hat{\mathbf{k}} \times \mathbf{u} = -\nabla_z p + \boldsymbol{\tau}_z + \mathbf{a}, \tag{3}$$

where $\hat{\mathbf{k}}$ is the upward unit vector, $\mathbf{u}$ is the horizontal velocity, f is the Coriolis parameter, p is the potential for the pressure gradient acceleration with $\nabla_z p$ its horizontal gradient, $\boldsymbol{\tau}_z$ is the vertical stress divergence, and $\mathbf{a}$ captures all remaining terms (including tendency, advection, and lateral friction). Specifically, $p = \tilde{p}/\rho_0$, where $\tilde{p}$ is the pressure and ρ_0 is the Boussinesq reference density. Similarly, let $g = \tilde{g}/\rho_0$, where $\tilde{g}$ is the gravitational acceleration. We now vertically integrate Eq. (3) from $-H$ to η:

$$f\hat{\mathbf{k}} \times \mathbf{U} = -(\eta\nabla p_s + H\nabla p_b + \nabla\chi) + \boldsymbol{\tau}_s - \boldsymbol{\tau}_b + \mathbf{A}, \tag{4}$$

where $p_s = p|_{z=\eta}$ and $p_b = p|_{z=-H}$ are the surface and bottom pressures (scaled by ρ_0),

$$\chi = g\int_{-H}^{\eta} z\rho\, dz \tag{5}$$

is the potential energy (scaled by ρ_0) relative to $z = 0$ and is a measure of the baroclinicity of the flow, $\boldsymbol{\tau}_s = \boldsymbol{\tau}|_{z=\eta}$ and $\boldsymbol{\tau}_b = \boldsymbol{\tau}|_{z=-H}$ are the surface and bottom frictional stresses, and $\mathbf{A} = \int_{-H}^{\eta} \mathbf{a}\, dz$. To obtain Eq. (4), we manipulated the vertically integrated pressure gradient acceleration using the Leibniz integral rule, integration by parts, and hydrostatic balance, $\partial_z p = -g\rho$, as

$$\int_{-H}^{\eta} \nabla_z p\, dz = \nabla\left(\int_{-H}^{\eta} p\, dz\right) - p_s\nabla\eta - p_b\nabla H \tag{6a}$$

$$= \nabla\left[p_s\eta + p_b H - \int_{-H}^{\eta} z(-g\rho)\, dz\right] - p_s\nabla\eta - p_b\nabla H \tag{6b}$$

$$= \eta\nabla p_s + H\nabla p_b + \nabla\chi. \tag{6c}$$

A brief mathematical interlude is needed. In Eq. (3), all terms are 3D vector fields with zero vertical ($\hat{\mathbf{k}}$) component. In contrast, all terms in Eq. (4) are 2D vector fields; e.g., ∇p_s is a 2D vector field since p_s is a scalar field in 2D space. If $\hat{\mathbf{k}} = (0, 0, 1)$ is a 3D vector field and $\mathbf{U} = (U, V)$ is a 2D vector field, the usual cross product between these variables is

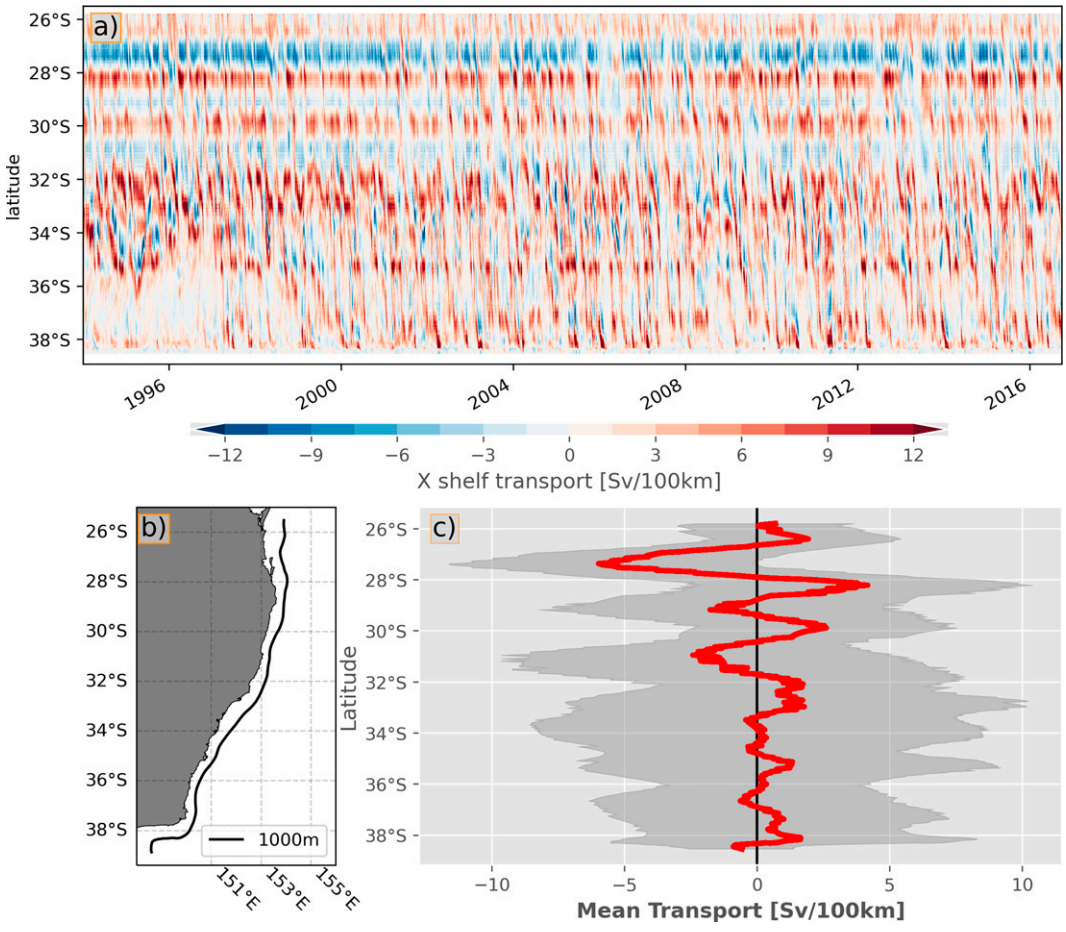

FIG. 5. Cross-shelf transport across the 1000-m isobath in the EAC system, showing (a) Hovmöller plot of cross-shelf transport, (b) location of the 1000-m isobath, and (c) time mean (red) and standard deviation (shaded) of cross-shelf transport. In (a) and (c), cross-shelf volume transport is given in units of Sv per 100 km of latitude.

undefined. Instead, we use $\hat{\mathbf{k}} \times \mathbf{U}$ as special notation, defined as follows. Let $\mathbf{U}_3$ denote the embedding of the 2D vector field $\mathbf{U}$ into 3D space: $\mathbf{U}_3 = (U, V, 0)$. Similarly, let $\mathbf{v}_2$ denote the projection of a 3D vector field $\mathbf{v} = (u, v, w)$ into 2D space: $\mathbf{v}_2 = (u, v)$. Now we define the 90° counterclockwise rotation, the curl of a 2D vector field, and the cross product of two 2D vector fields, as, respectively,

$$\hat{\mathbf{k}} \times \mathbf{U} \equiv (\hat{\mathbf{k}} \times \mathbf{U}_3)_2 = (-V, U), \tag{7a}$$

$$\nabla_2 \times \mathbf{U} \equiv \hat{\mathbf{k}} \cdot \nabla \times \mathbf{U}_3 = \partial_x V - \partial_y U, \tag{7b}$$

$$\boldsymbol{\mu} \times \mathbf{U} \equiv \hat{\mathbf{k}} \cdot (\boldsymbol{\mu}_3 \times \mathbf{U}_3) = \mu V - \nu U \tag{7c}$$

where $\boldsymbol{\mu} = (\mu, \nu)$ here. These rules allow us to apply many familiar rules from 3D vector calculus to 2D vectors. The following identities, with ϕ any (smooth) scalar field in 2D space, will be useful:

$$\nabla_2 \times \nabla\phi = 0, \tag{8a}$$

$$\nabla_2 \times (\phi\mathbf{U}) = \phi(\nabla_2 \times \mathbf{U}) + \nabla\phi \times \mathbf{U}, \tag{8b}$$

$$\boldsymbol{\mu} \cdot \mathbf{U} = \boldsymbol{\mu} \times (\hat{\mathbf{k}} \times \mathbf{U}), \tag{8c}$$

$$\nabla \cdot (\phi\mathbf{U}) = \nabla_2 \times (\phi\hat{\mathbf{k}} \times \mathbf{U}). \tag{8d}$$

Hughes and Killworth (1995) discuss the useful equations that result from dividing the depth-integrated momentum equation by 1, H, or f, and then taking its curl. Following the first option, taking the curl of Eq. (4) eliminates the $\nabla\chi$ term and yields an equation for the vorticity of the depth-integrated flow (also called the barotropic vorticity equation),

$$\mathbf{U} \cdot \nabla f = \nabla_2 \times (-\eta\nabla p_s - H\nabla p_b + \boldsymbol{\tau}_s - \boldsymbol{\tau}_b + \mathbf{A}) + f\eta_t, \tag{9}$$

having used Eqs. (8d) and (1). Equation (9) is a diagnostic equation for transport across f contours (latitude circles). This classic equation reduces to the even more classic Sverdrup balance $\beta V = \nabla_2 \times \boldsymbol{\tau}_s$ $\beta V = \nabla_2 \times \boldsymbol{\tau}_s$ (with $\beta = df/dy$) in a special limit that, most principally, requires constant H.

Next, following the second suggestion of Hughes and Killworth (1995), dividing Eq. (4) by H and then taking the

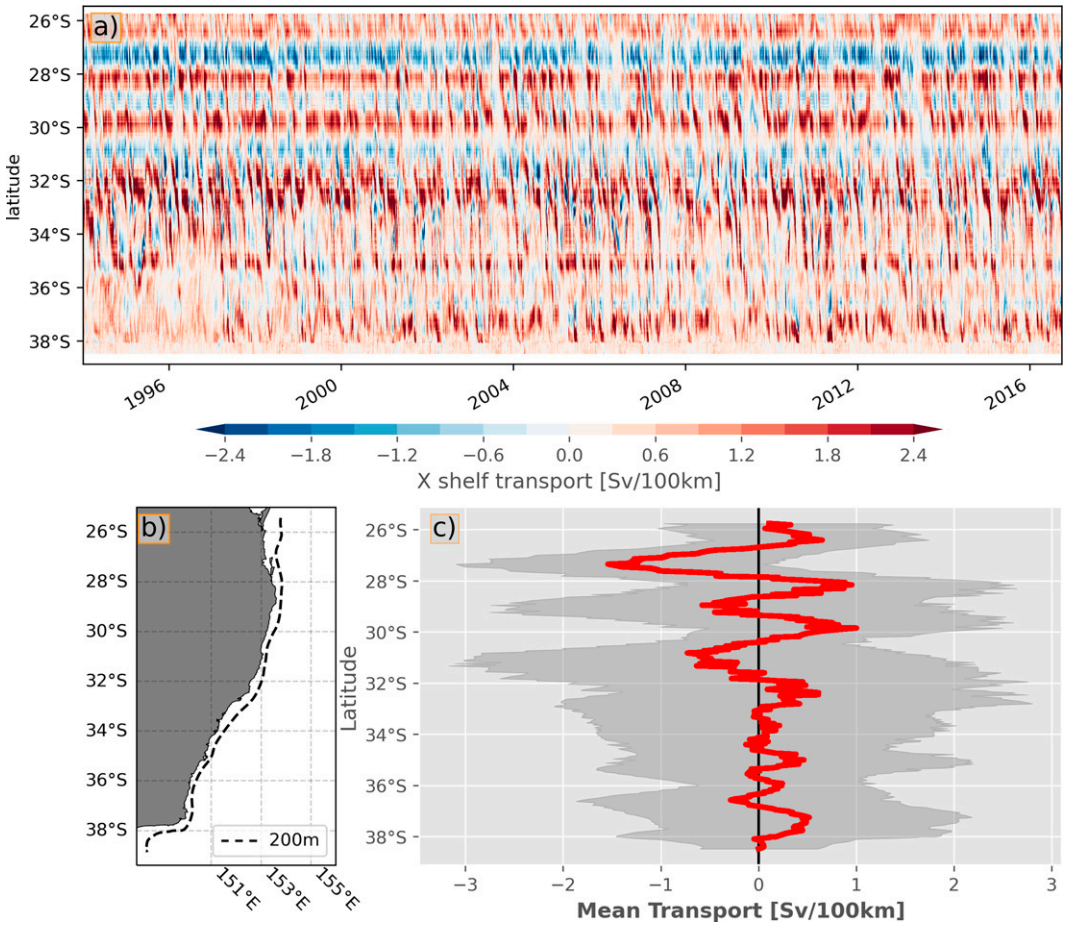

FIG. 6. Cross-shelf transport across the 200-m isobath in the EAC system, showing (a) Hovmöller plot of cross-shelf transport, (b) location of the 200-m isobath, and (c) time mean (red) and standard deviation (shaded) of cross-shelf transport. In (a) and (c), cross-shelf volume transport is given in units of Sv per 100 km of latitude.

2D curl eliminates the $(H\nabla p_b)/H$ term and yields an equation for the vorticity of the depth-averaged flow (also called the barotropic potential vorticity equation),

$$\mathbf{U}\cdot\nabla\left(\frac{f}{H}\right)=\nabla_2\times\left[-\frac{\eta}{H}\nabla p_s-\frac{1}{H}\nabla\chi+\frac{1}{H}(\boldsymbol{\tau}_s-\boldsymbol{\tau}_b+\mathbf{A})\right]+\frac{f}{H}\eta_t, \tag{10}$$

again using Eqs. (8d) and (1). Equation (10) is a diagnostic equation for transport across f/H contours (barotropic potential vorticity contours). The term $\nabla_2\times(H^{-1}\nabla\chi)$ is nonzero when bathymetric contours (H) are misaligned with contours of χ, and so is known as the joint effect of baroclinicity and relief (JEBAR; Sarkisyan and Ivanov 1971).

Physically, it is the bottom geostrophic flow that interacts with the bottom topography to produce a vertical velocity via the no-normal flow boundary condition, and the vortex stretching imposed by this bottom velocity appears in the barotropic vorticity equation, Eq. (9) via the bottom pressure torque. In Eq. (10), the JEBAR term arises because the vertically averaged geostrophic velocity is made to interact with the bottom topography. Correcting for this unphysical interaction, JEBAR can be interpreted in terms of topographic interactions with the difference between the bottom geostrophic flow and the vertically averaged geostrophic flow (Mertz and Wright 1992). This understanding of JEBAR as a correction for an unphysical process forms the basis for a prominent critique of JEBAR, as argued by Cane et al. (1998): JEBAR can be a large term in Eq. (10) even in cases where the topographic form drag, i.e., the pressure force exerted by the bottom topography on the flow, is precisely zero. For example, consider a layer of dense, stationary fluid that occupies the ocean up to the level of the highest (nonvertical) bathymetry. With nonstationary flow above this level, the flow is baroclinic and JEBAR can be large, despite there being no interaction between the flow and the topography. Our case of cross-shelf transport is analogous: a shallow current can cross deep isobaths, leading to a nonzero cross-shelf transport that is, in our vertically integrated analysis, every bit as valid as the cross-shelf transport created by a barotropic current. Thus, for our purposes, we do not consider this a drawback of JEBAR.

For small study regions where f varies far less than H in relative terms, Eq. (10) can serve as an approximate equation to study the cross-shelf transport. However, the EAC stretches meridionally over a vast region, from 26° to 38°S, meaning that f varies by 33% (relative to its value at 32°S). A diagnostic equation for flow across H contours, rather than f/H contours, is therefore preferred.

To obtain such a diagnostic equation for the cross-shelf transport, we can deviate from the manipulations suggested by Hughes and Killworth (1995), and instead take a new approach, dividing Eq. (4) by (fH) and then taking the 2D curl to obtain

$$\mathbf{U}\cdot\nabla H^{-1} = \nabla_2\times\left[-\frac{\eta}{fH}\nabla p_s - \frac{1}{f}\nabla p_b - \frac{1}{fH}\nabla\chi + \frac{1}{fH}(\boldsymbol{\tau}_s - \boldsymbol{\tau}_b + \mathbf{A})\right] + \frac{1}{H}\eta_t. \tag{11}$$

Defining $\hat{\mathbf{n}} = \nabla H/|\nabla H|$, the cross-shelf transport in the direction of increasing seafloor depth is

$$\mathbf{U}\cdot\hat{\mathbf{n}} = (\mathbf{U}\cdot\nabla H^{-1})\left(\frac{-H^2}{|\nabla H|}\right), \tag{12}$$

and hence may be diagnosed from Eq. (11) with a simple rescaling of the right-hand side by $-H^2/|\nabla H|$.

A different formulation of the (scaled) cross-shelf transport budget can be obtained directly from Eq. (12). Starting with $\mathbf{U}\cdot\nabla H^{-1}$, applying Eq. (8c) turns this into $\nabla H^{-1}\times(\hat{\mathbf{k}}\times\mathbf{U})$, then substituting in Eq. (4) yields

$$\mathbf{U}\cdot\nabla H^{-1} = f^{-1}\nabla H^{-1}\times(-\eta\nabla p_s - H\nabla p_b - \nabla\chi + \boldsymbol{\tau}_s - \boldsymbol{\tau}_b + \mathbf{A}). \tag{13}$$

This can be re-expressed, using Eq. (8b), as

$$\mathbf{U}\cdot\nabla H^{-1} = \frac{1}{f}\nabla_2\times\left[-\frac{\eta}{H}\nabla p_s - \frac{1}{H}\nabla\chi + \frac{1}{H}(\boldsymbol{\tau}_s - \boldsymbol{\tau}_b + \mathbf{A})\right] - \frac{1}{fH}\nabla_2\times(-\eta\nabla p_s - H\nabla p_b + \boldsymbol{\tau}_s - \boldsymbol{\tau}_b + \mathbf{A}). \tag{14}$$

Reminiscent of the depth-integrated and depth-averaged vorticity equations, the bottom pressure torque is eliminated in the top line, and JEBAR is eliminated in the bottom line. Indeed, Eq. (14) can be also obtained by combining the depth-averaged and depth-integrated vorticity budgets Eqs. (10) and (9): noting that $\nabla H^{-1} = f^{-1}\nabla(f/H) - (fH)^{-1}\nabla f$, the linear combination $f^{-1} - (fH)^{-1}$ yields Eq. (14) and eliminates the η_t terms.

We will use Eq. (14) to analyze the dynamic drivers of cross-shelf transport in our model. Next, we discuss the reasons to prefer Eq. (14) over Eq. (11) for this task, but readers who are primarily interested in the results may skip to section 4b.

Relative to Eq. (11), the advantage of Eqs. (13) and (14) is that they do *not* pack many terms together into a term involving $\nabla\cdot\mathbf{U} = -\eta_t$. This means that the transport $\mathbf{U}$ can be decomposed, from Eq. (4), into a sum of flows with distinct drivers, and the (scaled) cross-shelf transport associated with each of these components is correctly diagnosed in Eqs. (13) and (1), simply by its projection onto $\hat{\mathbf{n}}$ or ∇H^{-1}. For example, the Ekman transport $\mathbf{U}_{\mathrm{Ek}} = -f^{-1}\hat{\mathbf{k}}\times\boldsymbol{\tau}_s$ is the transport driven by $\boldsymbol{\tau}_s$, and its (scaled) cross-shelf transport is

$$\mathbf{U}_{\mathrm{Ek}}\cdot\nabla H^{-1} = \nabla H^{-1}\times(\hat{\mathbf{k}}\times\mathbf{U}_{\mathrm{Ek}}) \tag{15a}$$

$$= \nabla H^{-1}\times(f^{-1}\boldsymbol{\tau}_s) \tag{15b}$$

$$= f^{-1}\nabla_2\times(H^{-1}\boldsymbol{\tau}_s) - (H^{-1}\boldsymbol{\tau}_s)^{-1}\nabla_2\times\boldsymbol{\tau}_s, \tag{15c}$$

as appears in Eqs. (13) and (14). In contrast, it is incorrect to take $\nabla_2\times[(fH)^{-1}\boldsymbol{\tau}_s]$ from Eq. (11) as the (scaled) cross-shelf transport driven by $\boldsymbol{\tau}_s$, because $\mathbf{U}_{\mathrm{Ek}}$ has nonnegligible divergence, which combines with the divergences of other components to produce the negligible term $H^{-1}\eta_t$ in Eq. (11). That is, $\nabla_2\times[(fH)^{-1}\boldsymbol{\tau}_s] = \nabla\cdot(H^{-1}\mathbf{U}_{\mathrm{Ek}}) = \mathbf{U}_{\mathrm{Ek}}\cdot\nabla H^{-1} + H^{-1}(\nabla\cdot\mathbf{U}_{\mathrm{Ek}})$; the second term in the last expression is not negligible.

The dominant transport component is the geostrophic transport, which we can further decompose into baroclinic and barotropic components. One common definition of the barotropic flow is the depth-mean flow extended uniformly over a depth $H + \eta$, but then the baroclinic component has zero transport—in any direction, not just the cross-shelf direction—so this is not a useful decomposition for our purposes. Instead, we decompose the geostrophic transport into

1) the barotropic geostrophic transport defined as $\mathbf{u}_{gb}H$, i.e., the bottom geostrophic flow extended vertically over a distance H, and
2) the remainder, which is the baroclinic geostrophic transport from $z = -H$ to $z = 0$ plus the total geostrophic transport from $z = 0$ to η.

To better understand component 1, consider the bottom geostrophic flow $\mathbf{u}_{gb}$, which satisfies

$$f\hat{\mathbf{k}}\times\mathbf{u}_{gb} = -\nabla_z p|_{z=-H} = -(\nabla p_b - \rho_b g\nabla H), \tag{16}$$

where $\rho_b = \rho|_{z=-H}$ is the bottom in situ density. The transport of the barotropic geostrophic component 1 is $H\mathbf{u}_{gb}$ and its (scaled) cross-shelf transport is

$$H\mathbf{u}_{gb}\cdot\nabla H^{-1} = \nabla H^{-1}\times(\hat{\mathbf{k}}\times H\mathbf{u}_{gb}) \tag{17a}$$

$$= \left(\frac{-1}{H^2}\nabla H\right)\times(-\nabla p_b + \rho_b g\nabla H)\frac{H}{f} \tag{17b}$$

$$= \frac{1}{fH}\nabla_2\times(H\nabla p_b). \tag{17c}$$

Thus, the bottom pressure torque term in Eq. (14) is the cross-shelf transport caused by component 1. This is readily understood: in Eq. (17b), the transport $H\mathbf{u}_{gb}$ is decomposed into a flow along p_b contours and a flow along H contours; the latter, by definition, produces no cross-shelf transport, while the former produces cross-shelf transport wherever the p_b contours are misaligned with the H contours, i.e., when the bottom pressure torque is nonzero.

The (scaled) cross-shelf transport due to the geostrophic component 2 is simply the p_s and χ terms in Eq. (14) that arise from the pressure gradient. To understand these better, note that

$$\nabla\chi = \rho_s g\eta\nabla\eta - \rho_b gH\nabla H + g\int_{-H}^{\eta} z\nabla_z\rho\, dz \qquad (18)$$

via the Leibniz integral rule. Consider the right-hand side of Eq. (18): the last term gives the total baroclinic geostrophic transport; the first term combines with the $\eta\nabla p_s$ term in Eq. (13) to give the (scaled) cross-shelf transport due to the surface geostrophic flow extended over a distance η; the middle term is part of the bottom geostrophic flow and generates precisely zero cross-shelf transport. However, this decomposition of $\nabla\chi$ undesirably separates component (ii) into subcomponents (the total baroclinic geostrophic transport and the surface geostrophic transport between $z = 0$ and η) that have nonzero curl, which would manifest when going from Eqs. (13) to (14). In our system, the surface geostrophic transport between $z = 0$ and η is negligible compared to the total baroclinic geostrophic transport, so we leave $\nabla\chi$ undecomposed, and use Eq. (14) as our primary diagnostic equation.

b. Results

To explore the role of each of the terms in Eq. (14), we calculate the contributions to the cross-shelf transport using diagnostic output from EAC-ROMS for the depth-averaged lateral momentum equation. Due to resource constraints we did not run the momentum budget for the full 22 years, and instead use the years from 2010 to 2015. Figure A1 in the appendix shows that use of this 5-yr period is consistent with the longer 22-yr period used elsewhere. As our analysis is restricted to the mean state, we assume that the mean momentum balance [Eq. (14)] driving this mean cross-shore transport is also consistent over the 5- and 22-yr periods.

Numerically, we first multiply the depth-averaged lateral momentum diagnostics by $\eta + H$ averaged onto the U and V grids, as the model does, to obtain the depth-integrated lateral momentum terms. Next, we decompose the pressure gradient acceleration as in Eq. (6a), with the model diagnostic providing the left-hand side of Eq. (6a). We directly calculate the surface and bottom pressure terms by averaging η and H onto the U and V grid and by taking first differences of p_s and p_b. Then, we take the baroclinic term $\nabla\chi$ as a residual. Next, we take the curl of these diagnostics to obtain the depth-integrated vorticity terms, which we then divide by f and H (both averaged onto the vorticity grid from four surrounding tracer grid points) to obtain the bottom line of Eq. (14). Similarly, we divide these diagnostics by H (averaged onto the U and V grids) then take the curl to obtain the depth-averaged vorticity terms, which we then divide by f (again, averaged onto the vorticity grid) to obtain the top line of Eq. (14). Applying both of these operations to the Coriolis diagnostic term and subtracting yields the scaled cross-shelf transport, $\mathbf{U}\cdot\nabla H^{-1}$ via Eq. (8d) on the left-hand side of Eq. (14). Finally, we scale everything by $-H^2/|\nabla H|$, with H averaged onto the vorticity grid as above, and with $|\nabla H|$ obtained by squaring the first differences of H on the U and V grids, then interpolating these onto the vorticity grid, summing, and taking the square root. Crucially, our numerics satisfy the vector identity $\nabla_2\times(H^{-1}\nabla H) = 0$, so that the bottom pressure torque, $\nabla_2\times(H^{-1}\nabla p_b)$ is independent of the passive part of the bottom pressure, namely, $gH\rho_0$ for an arbitrary density ρ_0.

Figure 7 shows the contributions of the χ (JEBAR), bottom pressure torque, surface stress, bottom stress, and nonlinear advection terms to the time-mean cross-isobath transport Eq. (14). The other terms, namely, those due to surface pressure, tendency, and lateral viscosity, are negligible and hence not shown. The terms are multiplied by the scale factor $-H^2/|\nabla H|$ as per Eq. (12), giving units of $m^2\ s^{-1}$, then multiplied by 0.1 to get Sv per 100 km (consistent with previous figures). To highlight the shelf region, the terms are plotted on axes of distance offshore from the coast and latitude.

We now examine the various cross-shelf transport terms at the 1000-m isobath. The cross-shelf transport calculated from the Coriolis term in the online momentum equation diagnostic, i.e., the left-hand side of Eq. (14), produces cross-shelf transport values (Figs. 7a,b) consistent in magnitude and sign with those calculated using Eq. (2) barring some small (<1 Sv per 100 km) isolated differences where the shelf edge is particularly steep (These differences arise because of model numerics, time-averaging and the need to interpolate between the separate locations of the two velocity components on an Arakawa C grid.). The χ term (Fig. 7c), which accounts for baroclinic geostrophic cross-shelf transport plus a small contribution from the surface geostrophic flow, is 5 times greater in magnitude than the other terms of the balance, dominating the cross-shelf transport, particularly between the 200- and 1000-m isobaths. The second most important contribution comes from direct interaction between the flow and the bathymetry via the bottom pressure torque (Fig. 7d), which accounts for cross-shelf transport driven by the bottom geostrophic flow. The dominance of these two terms together implies that cross-shelf transport in this region is predominantly geostrophic. The balance of terms is in broad agreement with the observational cross-shelf momentum balance calculated at 30°S by Schaeffer et al. (2013), who find geostrophy dominates, with secondary contributions from bottom stress and nonlinear advection. Between 26° and 30°S, the cross-shelf transport driven by χ covaries strongly with the bathymetry and drives onshore transport on the upstream side of the maxima in shelf width (at 28° and 29.5°S) and offshore transport on the downstream (lee) side. In other words, the cross-shelf transport here is associated with meanders in the isobaths underneath the baroclinic EAC jet that carries much of its transport high in the water column and so has little direct interaction with topography.

Bottom stress (Fig. 7e) has been documented to play an important role in local upwelling, through the bottom Ekman transport processes examined observationally by Roughan and Middleton (2002, 2004). The influence of these processes can be seen in zones of onshore transport at 29°–30°S and 31°–32°S, but bottom stress does not play a large role in the overall cross-shelf transport.

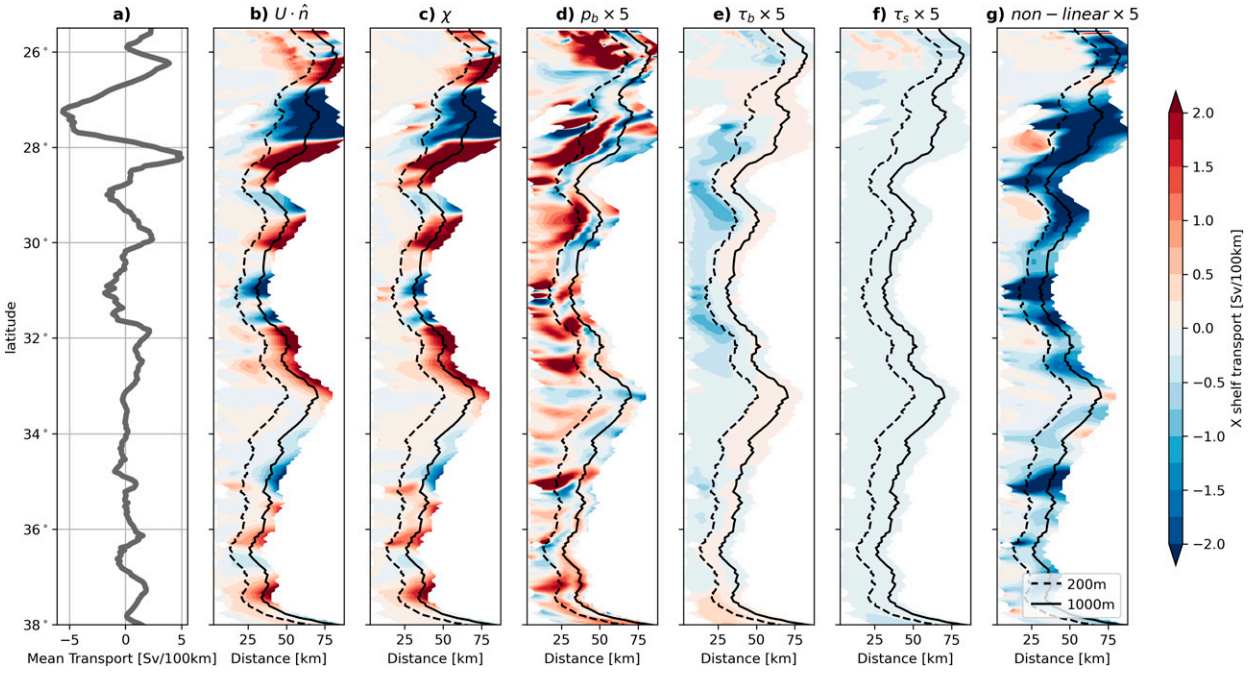

FIG. 7. Time mean of the dominant terms in the cross-isobath volume transport budget (Sv per 100 km of latitude), namely, $-H^2/|\nabla H|$ times Eq. (14). Positive (red) values indicate offshore transport. (a) The cross-shelf transport $\mathbf{U} \cdot \hat{\mathbf{n}}$ at the 1000-m isobath, (b) the cross-shelf transport $\mathbf{U} \cdot \hat{\mathbf{n}}$, and the cross-shelf transports driven by (c) the baroclinic geostrophic flow (χ), (d) the bottom pressure torque (p_b), (e) the bottom stress ($\boldsymbol{\tau}_b$), (f) the surface stress ($\boldsymbol{\tau}_s$), and (g) the vertically integrated nonlinear advection ($\int_{-H}^{\eta} \mathbf{u} \cdot \nabla \mathbf{u} + w\mathbf{u}_z \, dz$). Note that the terms in (d)–(g) have been multiplied by a factor of 5 for clarity. Axes in (b)–(g) are distance offshore from the coast in kilometers and latitude. The 200- and 1000-m isobaths are shown by the dashed and solid contours, respectively.

The surface stress term (Fig. 7f) is notable for its lack of influence on the time-mean cross-shelf transport. This minor influence of wind on net cross-shelf transport had been hinted at in previous observational studies (Wood et al. 2012; Rossi et al. 2014), but here we are able to show the limited impact of surface stress across the whole EAC system. However, it is important to note that our analysis so far is restricted to the time-mean cross-shelf transport. The surface stress term could have a larger impact on cross-shelf transport variability, e.g., associated with higher-frequency atmospheric variability such as storms or the sea breeze.

At any single location, nonlinear advection (Fig. 7g) plays a small but not insignificant role in comparison to the geostrophic terms, χ and p_b. Nonlinear advection consistently drives onshore transport across the shelf break between the 200- and 1000-m isobaths over the length of the EAC system, rather than alternating between onshore and offshore transport as is the case for the χ and p_b terms. Inshore of the 200-m isobath (on the midshelf), cross-shelf transport due to nonlinear advection is much weaker and more variable. There is a local maximum in the magnitude of the nonlinear term (at 28°S) which occurs in an area which has high barotropic instabilities, indicating the shedding of anticyclonic eddies from the EAC jet (Li et al. 2021b). The exact drivers of the nonlinear term are difficult to diagnose, but in general it appears to be positive (pointing offshore) where bottom speeds are high (generally on the inshore edge of the jet) and negative (pointing onshore) where bottom speeds are lower, such as beneath the main EAC current core (Fig. 4). The importance of the consistent onshore transport driven by nonlinear advection is revealed when looking at the along-shelf integral (from 26° to 38°S) of the terms in Eq. (14) (Fig. 8). When integrated along the length of the shelf, the net onshore transport driven by nonlinear advection balances the net offshore transport associated with χ and bottom pressure torque at both the 200- and 1000-m isobaths. This balance shows the importance of nonlinear advection in maintaining the overall shelf mass balance. The role of nonlinear advection in driving cross-shelf transport is not well understood in the literature, and this term is often neglected for simplicity in studies of the momentum balance (Everett et al. 2012; Cetina-Heredia et al. 2014; Oke et al. 2019). Also notable in Fig. 8 is the increase in the importance of bottom pressure torque at the 200-m isobath compared to at 1000 m. This indicates that cross-shelf transport becomes more barotropic and direct topographic interactions become more important in the shallower water closer to the shelf.

5. Exploring time-varying cross-shelf transport

In addition to varying spatially along the coast, the cross-shelf volume transport is also highly variable in time (Figs. 5a and 6a). Onshore transport between 27° and 28°S, responsible for the transport of almost 4 Sv of water onto the shelf, is

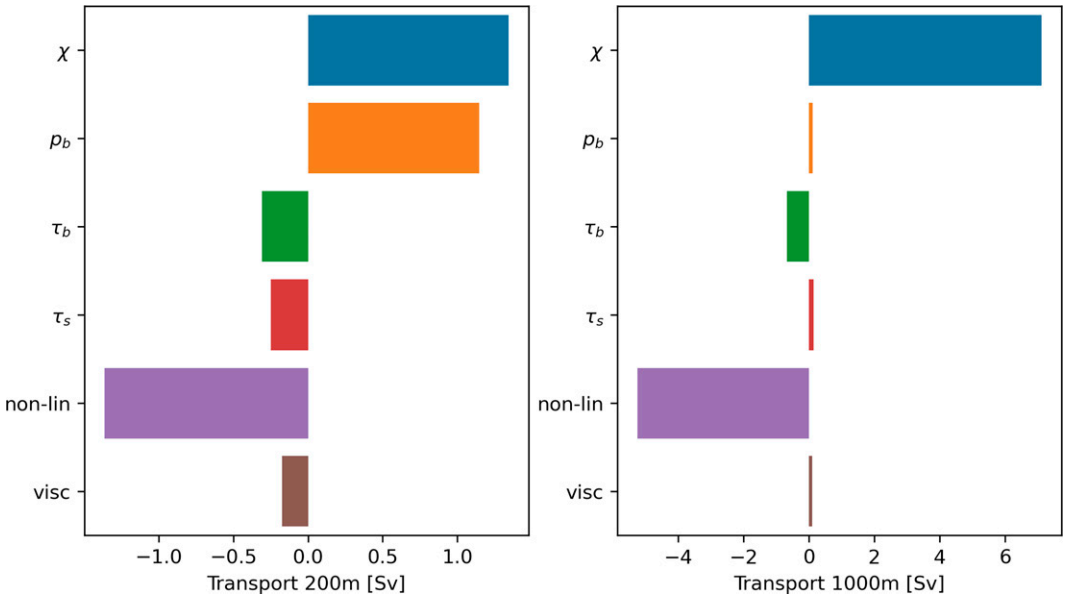

FIG. 8. Time mean of dominant terms of the cross-isobath volume transport budget, Eq. (14), integrated from 26° to 38°S, along the 200- and 1000-m isobaths.

highly persistent. The return of this water offshore at 28°S is also semipermanent, with the notable exception of short events, such as those in 2007 or 2013, where the flow structure is interrupted for a period of approximately 2 months (Fig. 5a). As the EAC flows poleward from 28° to 32°S, the alternating spatial peaks of onshore and offshore transport (visible in both the time-mean and cumulative sum of cross-shelf transport; Figs. 5c, 6c, and 3b) reduce in magnitude, as does the poleward shelf transport (Fig. 3a), while variability increases in the poleward direction (Figs. 5c and 6c). Poleward of 32°S, the magnitude of the time-mean cross-shelf transport is less than a quarter of that observed upstream. However, the variability remains high (Figs. 5c and 6c), and the time-invariant alternating pattern of onshore–offshore volume transport bands observed between 26° and 32°S is no longer present, with cross-shelf transport becoming more variable in both magnitude and sign.

As it is known that mesoscale eddies dominate the flow in the EAC southern extension (Everett et al. 2012; Cetina-Heredia et al. 2014; Oke et al. 2019), it is useful to decompose the variability by time scale. When filtered to retain variability in the mesoscale time band [taken here as 60–200 days, following

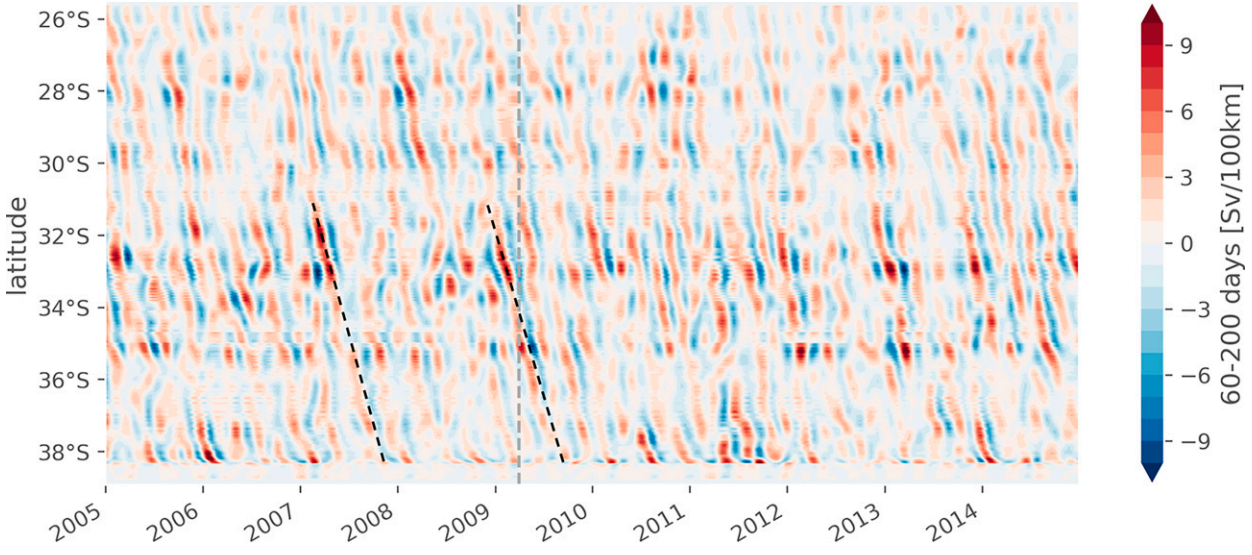

FIG. 9. Hovmöller plot of cross-shelf transport anomalies (Sv per 100 km) bandpass filtered from 60 to 200 days, across the 1000-m isobath between 2005 and 2015. The gray dashed line shows the timing of the case study in Fig. 11 and the black dashed lines show propagation of anomalies due to mesoscale eddies at a speed of approximately 1.85 km day^{-1}.

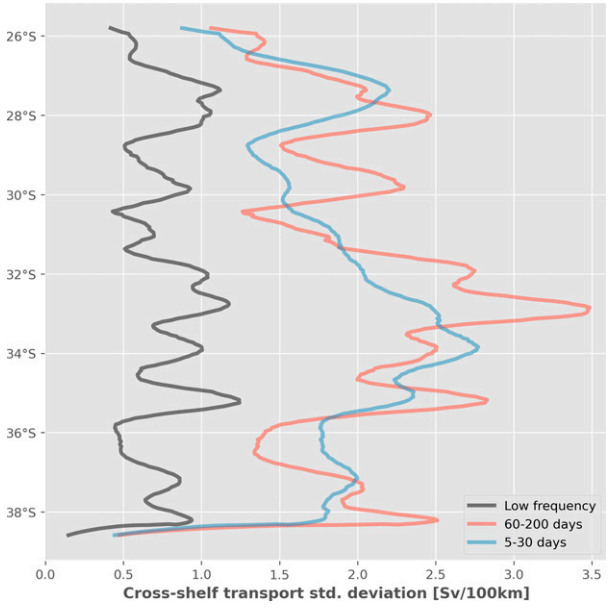

FIG. 10. Standard deviation of cross-shelf transports (Sv per 100 km) partitioned into low frequency (>730 days), mesoscale (60–200 days) and weather band (5–30 days) time scales.

Kerry and Roughan (2020)], the cross-shelf transport is characterized by events that propagate poleward along the length of the system (Fig. 9, highlighted by black dashed lines). These events are most intense between 32° and 35°S and propagate at a rate of 0.5° of latitude per month, which equates to an eddy advection speed of approximately ~1.85 km day^{-1}. This speed is consistent with the propagation rate of eddies observed in this region (Pilo et al. 2015). Variability in the mesoscale time band increases in magnitude poleward of 32°S (from 2 to 3.5 Sv per 100 km), with a peak at 33°S and secondary peaks at 28° and 35°S (Fig. 10). In contrast, variability at low frequencies (>2 years) is relatively small and uniform with latitude. The strongest cross-shelf transport events in the mesoscale band (Fig. 9) occur at the same latitude (33°S) as the median position of eddy dipoles in the EAC separation zone. These counterrotating paired eddy structures have been observed to drive strong jets directed toward the coast (Malan et al. 2020; Archer et al. 2020) which deliver biota to the shelf (Cetina-Heredia et al. 2019a). These eddy dipoles result in a maximum of onshore transport variability at mesoscale frequencies at 33°S (Fig. 10). The secondary peak in cross-shelf transport variability amplitude in the mesoscale time band at 28°S also occurs in a known area of cyclonic eddy activity (Li et al. 2021b), although the signal is more complex here due to the strong time-mean onshore transport associated with the acceleration of the EAC.

At the 5–30-day time scale, chosen to represent the "weather band" where storm events and smaller instabilities such as frontal eddies could drive cross-shelf transport, maxima in variability occur at 27° and 34°S (blue line in Fig. 10). The link of this maxima in cross-shelf transport at 27°S at a 5–30-day time scale to frontal eddy activity is consistent with Azis Ismail and Ribbe (2019) who report frontal eddies exporting order 1 Sv of shelf water at time scales ranging from 7 to 38 days. As frontal eddy activity has been observed along the length of the EAC system (Ribbe and Brieva 2016; Schaeffer and Roughan 2017; Roughan et al. 2017), the presence of small frontal eddies could account for the variability in cross-shelf exchange of 1–3 Sv per 100 km from 26° to 38°S (Fig. 10). An example of one of these small frontal eddies can be seen in Fig. 11a between 35° and 36°S, just offshore of the 1000-m isobath.

The understanding of the dynamical conditions associated with cross-shelf transport in different parts of the EAC system described above is exemplified in a snapshot of SST and SSH, along with the associated cross-shelf transport (Fig. 11). This scenario shows a peak in onshore transport at 27°S and alternating patterns in the "jet regime" consistent with the time-mean cross-shelf transport patterns shown in Figs. 5c and 6c. However, the largest onshore transport actually occurs at 33°S. As noted above, this onshore transport is associated with a counterrotating eddy dipole structure, which drives flow directly onshore. Notably, the interaction of the anticyclonic part of the eddy–dipole pair (centered at 35°S) with the shelf break can be seen in the deformation in shape of the sea surface height contour which changes from circular to more elongated where it crosses the shelf break at 33°S. This deformation occurs where onshore transport is largest and is consistent with the findings of Cetina-Heredia et al. (2019a) that eddies leak water when their shape is changed as they interact with the shelf break. The details of how cross-shelf transport is driven by the differing mechanisms of EAC jet bathymetry as well as eddy–eddy–shelf interaction, one mostly time invariant and the other highly time variant, are evident in this single snapshot of the EAC system.

6. Summary and implications

In this study we have used a high-resolution regional model to explore the spatial structure and dynamical drivers of vertically integrated cross-shelf transport in the EAC system. We identified two separate regimes of cross-shelf volume transport, associated with the dominant geostrophic flow pattern. The EAC jet-dominated regime equatorward of 32°S is characterized by large spatially alternating time-mean cross-shelf transport and low variability. In contrast, south of 32°S in the eddy-dominated regime the time-mean cross-shelf transport is weak, but the variability is high. This clear difference in cross-shelf transport dynamics between the jet and eddy-dominated regions of the EAC may be useful for the interpretation of cross-shelf flows in other western boundary currents, which all feature eddy or jet dominated regions to some extent despite differing in their bathymetry, separation points, and total transport.

From our results, the relationship between the baroclinicity of the surface-intensified western boundary current jet and the depth of the shelf break appears important for the magnitude of cross-shelf volume transport in the jet region. This could lead to less cross-shelf transport in systems with a deeper jet, such as the Agulhas Current, where velocities exceed 0.5 m s^{-1} as deep as 1000 m—far deeper than the shelf break (Beal et al. 2015).

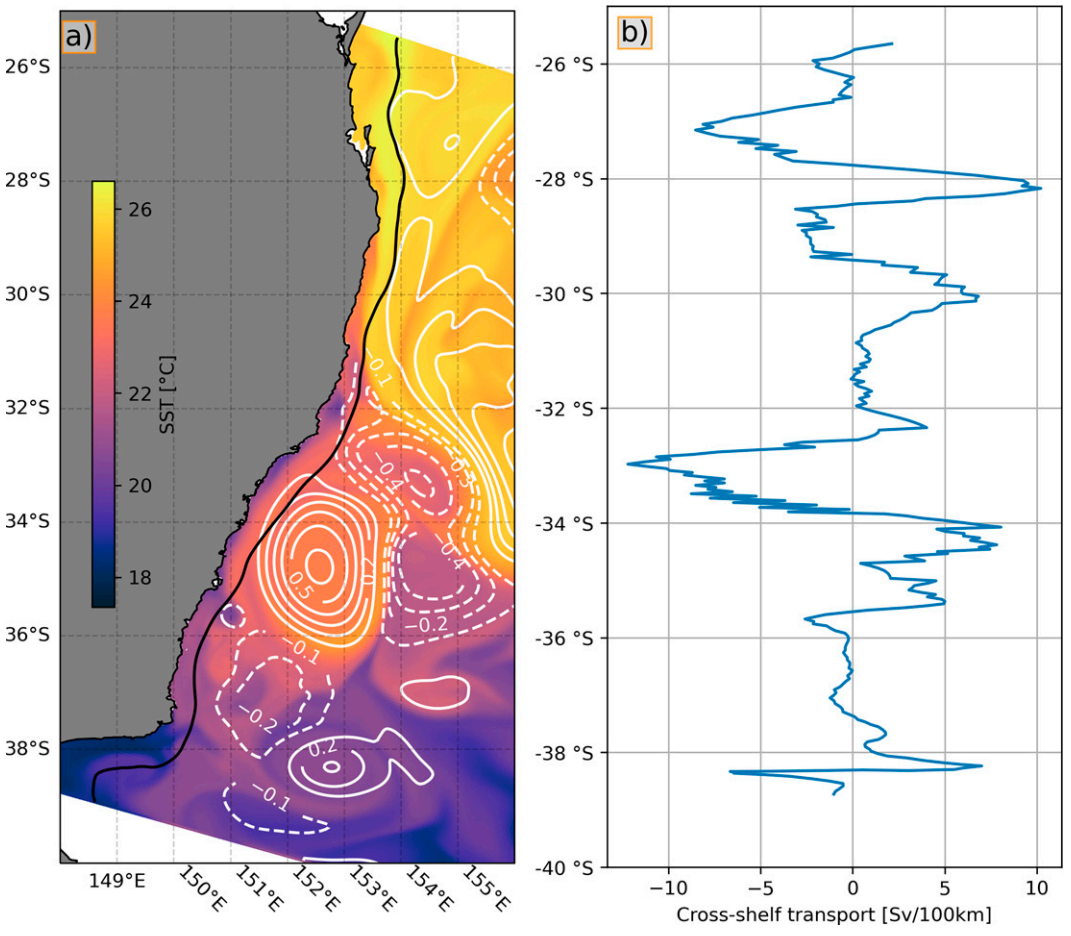

FIG. 11. Snapshot of (a) sea surface temperature (shaded) and sea surface height anomalies (contours at 0.1-m intervals, dashed contours indicate negative values), along with (b) cross-shelf transport across the 1000-m isobath, for the 1 Apr 2009.

To give context to the magnitudes of the time-mean cross-shelf transport, they can be compared to the mean alongshore transport of the EAC itself. We consider this comparison at the scale of 2° of latitude, a similar length scale used by Kerry and Roughan (2020) in calculating the EAC transport in the same ROMS domain. From 26° to 28°S, cross-shelf transport across the 1000-m isobath is 19% of the total EAC transport (18.97 Sv) while from 36° to 38°S, where time-mean cross-shelf transport is weakest, the cross-shelf transport is only 5% of the total EAC transport (17.05 Sv). Our results also expand on the earlier work of Ribbat et al. (2020). Both our study and Ribbat et al. (2020) find time-mean offshore transport of order 2 Sv per 100 km between 32° and 33°S, transitioning to very weak time-mean onshore transport at 34°S. Our results reveal that 32°–34°S is in fact one of the regions with the lowest time-mean cross-shelf transport in the EAC system and that the high variability of cross-shelf transport at this latitude is related to mesoscale eddy dipole events.

The momentum budget for cross-shelf transport reveals that cross-shelf flow is predominantly comprised of a baroclinic, geostrophic flow. Dynamically, this indicates most of the cross-shelf transport (~80%) is due to the meandering of the surface-intensified geostrophic EAC jet on and off the shelf. This kind of intrusion caused by a geostrophic western boundary current jet "overshooting" bathymetric protrusions also occurs north of Taiwan in the Kuroshio (Hsueh et al. 1996; Guo et al. 2006). While the Kuroshio bifurcates into the East China Sea, in the EAC this type of intrusion occurs twice: once at the protruding bathymetric feature at 28°S, and again at 29.5°S. The strength of the intrusion is dependent on the strength and vertical extent of the EAC jet itself. At 27°S the jet is narrow and shallow, with a large vertical shear of velocity in the top 1000 m of the water column (Kerry and Roughan 2020). This shallow baroclinicity allows the jet to meander relatively unconstrained onto the shelf, hence the large cross-shelf transport values at this latitude. As the EAC jet proceeds poleward it broadens and deepens (Kerry and Roughan 2020), becoming more barotropic and thus more constrained by the bathymetry, transporting less volume on and off the shelf. The pattern changes south of 32°S, the mean separation latitude of the EAC jet, where offshore transport occurs (at 33°S) as the EAC jet turns eastward and leaves the shelf. This marks the transition from the shelf region dominated by the EAC jet, to the more eddying regime of the EAC southern extension.

Direct topographic interactions, through the bottom pressure torque term, are also important as a secondary driver of cross-shelf transport, with their importance increasing at the shallower parts of the shelf break. The surface stress and bottom stress play negligible roles in the overall cross-shelf transport. The nonlinear advection term, while small at individual locations, is consistent in driving onshore transport along the length of the shelf break. When considering the whole length of the shelf, this means that nonlinear advection plays the primary role in balancing the net offshore transport of the baroclinic (χ) and bottom stress terms.

Recent work on trends in the EAC system has shown an increase in eddy kinetic energy (Li et al. 2021b), an increase in associated ocean heat content (Li et al. 2022) and a strong shelf warming trend (Malan et al. 2021). Furthermore, it has been suggested that shelf warming may be related to increased eddying. The eddy-driven cross-shelf transport results presented in section 5 provide a plausible mechanism via which trends in offshore eddying and shelf warming may be closely coupled in the eddy-dominated regime. However, cross-shelf heat transport (and trends) in the EAC system require further investigation.

The high level of eddy-driven variability poleward of EAC separation could have consequences for our understanding of carbon fluxes from the shelf to the deep ocean in this region. Macdonald et al. (2009) examined these dynamics using an idealized coupled physical–biological–chemical model and found that the EAC is a net sink for carbon poleward of its separation point. However, the model used in their study is only run for 21 days, and hence may only capture a single phase of the eddy-driven variability, which occurs on 60–200-day time scales (Bowen et al. 2005; Mata et al. 2006; Schaeffer et al. 2014; Kerry and Roughan 2020). In this paper we show that this eddy-driven shelf transport variability is large, and so if there are significant correlations between cross-shelf volume transport and dissolved carbon concentration, it may have a significant impact on the carbon uptake dynamics on the shelf poleward of 32°S.

This paper has quantified the cross-shelf transport along the length of the EAC system and provided explanations for the dominant patterns, distribution, and drivers of cross-shelf transport. Our results allow for improved interpretation and contextualization of earlier observations of cross-shelf flows. Our results also provide a context for future studies of cross-shelf variability of tracers such as heat and salt, or biological quantities such as nutrients, dissolved carbon, passive floating plankton, or eggs and larvae.

Acknowledgments. The EAC-ROMS model development was partially funded by Australian Research Council projects DP140102337 and LP160100162 to MR. NM acknowledges support from Australian Research Council Industry Linkage grant LP170100498. GJS and RMH acknowledge support from the Australian Research Council though grant FL150100090. This research was undertaken with the assistance of resources and services from the National Computational Infrastructure (NCI), which is supported by the Australian Government. This research also includes computations using the computational cluster Katana (2010) doi:10.26190/669X-A286, supported by Research Technology Services at UNSW Sydney.

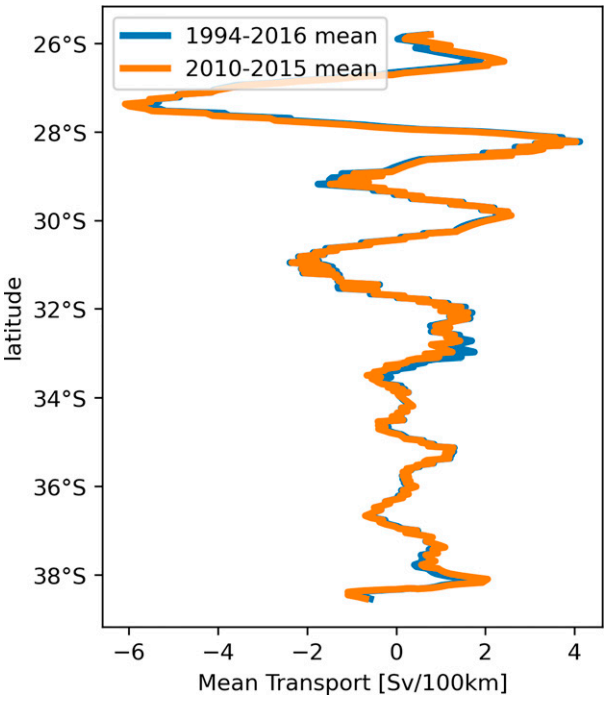

FIG. A1. Comparison of cross-shelf transport, calculated following Eq. (2), for the periods 1994–2016 and 2010–15. Results show that the chosen 5-yr period for the momentum budget analysis is a fair representation of the mean across the full 22-yr period.

Data availability statement. Model initial and boundary conditions are provided by CSIRO Australia BRAN2016 and available at https://research.csiro.au/bluelink/outputs/data-access/. The atmospheric forcing BARRA-R reanalysis were obtained from http://www.bom.gov.au/research/projects/reanalysis/. The tide forcing was obtained from https://www.tpxo.net/global/tpxo8-atlas. The EAC-ROMS model output (https://doi.org/10.26190/TT1Q-NP46) is available at https://researchdata.edu.au/high-resolution-22-version-20/1676421 and should be cited as Li et al. (2021a).

APPENDIX

Comparison between 1994–2016 and 2010–15 Time-Mean Cross-Shelf Transport

This appendix shows a comparison (Fig. A1) between the time-mean cross-shelf transport for the shorter 2010–15 time period used to diagnose the drivers of cross-shelf transport and the longer 1994–2016 period that is used in the rest of the paper.

REFERENCES

Archer, M. R., M. Roughan, S. R. Keating, and A. Schaeffer, 2017: On the variability of the East Australian Current: Jet structure, meandering, and influence on shelf circulation. *J. Geophys. Res. Oceans*, **122**, 8464–8481, https://doi.org/10.1002/2017JC013097.

——, A. Schaeffer, S. Keating, M. Roughan, R. Holmes, and L. Siegelman, 2020: Observations of submesoscale variability and frontal subduction within the mesoscale eddy field of the Tasman Sea. *J. Phys. Oceanogr.*, **50**, 1509–1529, https://doi.org/10.1175/JPO-D-19-0131.1.

Azis Ismail, M. F., and J. Ribbe, 2019: On the cross-shelf exchange driven by frontal eddies along a western boundary current during austral winter 2007. *Estuarine Coastal Shelf Sci.*, **227**, 106314, https://doi.org/10.1016/j.ecss.2019.106314.

——, ——, J. Karstensen, C. Lemckert, S. Lee, and J. Gustafson, 2017: The Fraser Gyre: A cyclonic eddy off the coast of eastern Australia. *Estuarine Coastal Shelf Sci.*, **192**, 72–85, https://doi.org/10.1016/j.ecss.2017.04.031.

Beal, L. M., S. Elipot, A. Houk, and G. M. Leber, 2015: Capturing the transport variability of a western boundary jet: Results from the Agulhas Current Time-Series Experiment (ACT). *J. Phys. Oceanogr.*, **45**, 1302–1324, https://doi.org/10.1175/JPO-D-14-0119.1.

Bowen, M. M., J. L. Wilkin, and W. J. Emery, 2005: Variability and forcing of the East Australian Current. *J. Geophys. Res.*, **110**, C03019, https://doi.org/10.1029/2004JC002533.

Brink, K. H., 2016: Cross-shelf exchange. *Annu. Rev. Mar. Sci.*, **8**, 59–78, https://doi.org/10.1146/annurev-marine-010814-015717.

Cai, W.-J., M. Dai, and Y. Wang, 2006: Air-sea exchange of carbon dioxide in ocean margins: A province-based synthesis. *Geophys. Res. Lett.*, **33**, L12603, https://doi.org/10.1029/2006GL026219.

Cane, M. A., V. M. Kamenkovich, and A. Krupitsky, 1998: On the utility and disutility of JEBAR. *J. Phys. Oceanogr.*, **28**, 519–526, https://doi.org/10.1175/1520-0485(1998)028<0519:OTUADO>2.0.CO;2.

Cenedese, C., R. E. Todd, G. G. Gawarkiewicz, W. B. Owens, and A. Y. Shcherbina, 2013: Offshore transport of shelf waters through interaction of vortices with a shelfbreak current. *J. Phys. Oceanogr.*, **43**, 905–919, https://doi.org/10.1175/JPO-D-12-0150.1.

Cetina-Heredia, P., M. Roughan, E. van Sebille, and M. A. Coleman, 2014: Long-termtrends in the East Australian current separation latitude and eddy driven transport. *J. Geophys. Res. Oceans*, **119**, 4351–4366, https://doi.org/10.1002/2014JC010071.

——, ——, G. Liggins, M. A. Coleman, and A. Jeffs, 2019a: Mesoscale circulation determines broad spatio-temporal settlement patterns of lobster. *PLOS ONE*, **14**, e0214996, https://doi.org/10.1371/journal.pone.0211722.

——, ——, E. van Sebille, S. Keating, and G. B. Brassington, 2019b: Retention and leakage of water by mesoscale eddies in the East Australian Current system. *J. Geophys. Res. Oceans*, **124**, 2485–2500, https://doi.org/10.1029/2018JC014482.

Cherian, D. A., and K. H. Brink, 2018: Shelf flows forced by deep-ocean anticyclonic eddies at the shelf break. *J. Phys. Oceanogr.*, **48**, 1117–1138, https://doi.org/10.1175/JPO-D-17-0237.1.

Combes, V., R. P. Matano, and E. Palma, 2021: Circulation and cross-shelf exchanges in the northern shelf region of the southwestern Atlantic: Kinematics. *J. Geophys. Res. Oceans*, **126**, e2020JC016959, https://doi.org/10.1029/2020JC016959.

Egbert, G. D., and S. Y. Erofeeva, 2002: Efficient inverse modeling of barotropic ocean tides. *J. Atmos. Oceanic Technol.*, **19**, 183–204, https://doi.org/10.1175/1520-0426(2002)019<0183:EIMOBO>2.0.CO;2.

Everett, J. D., M. E. Baird, P. R. Oke, and I. M. Suthers, 2012: An avenue of eddies: Quantifying the biophysical properties of mesoscale eddies in the Tasman Sea. *Geophys. Res. Lett.*, **39**, L16608, https://doi.org/10.1029/2012GL053091.

Guerrero, L., J. Sheinbaum, I. Mariño-Tapia, J. J. González-Rejón, and P. Pérez-Brunius, 2020: Influence of mesoscale eddies on cross-shelf exchange in the western Gulf of Mexico. *Cont. Shelf Res.*, **209**, 104243, https://doi.org/10.1016/j.csr.2020.104243.

Guo, X., Y. Miyazawa, and T. Yamagata, 2006: The Kuroshio onshore intrusion along the shelf break of the East China Sea: The origin of the Tsushima warm current. *J. Phys. Oceanogr.*, **36**, 2205–2231, https://doi.org/10.1175/JPO2976.1.

Hsueh, Y., H. -J. Lie, and H. Ichikawa, 1996: On the branching of the Kuroshio west of Kyushu. *J. Geophys. Res.*, **101**, 3851–3857, https://doi.org/10.1029/95JC03754.

Hughes, C. W., and P. D. Killworth, 1995: Effects of bottom topography in the large-scale circulation of the Southern Ocean. *J. Phys. Oceanogr.*, **25**, 2485–2497, https://doi.org/10.1175/1520-0485(1995)025<2485:EOBTIT>2.0.CO;2.

Kerry, C., and M. Roughan, 2020: Downstream evolution of the East Australian Current system: Mean flow, seasonal, and intra-annual variability. *J. Geophys. Res. Oceans*, **125**, e2019JC015227, https://doi.org/10.1029/2019JC015227.

——, B. Powell, M. Roughan, and P. Oke, 2016: Development and evaluation of a high resolution reanalysis of the East Australian Current region using the Regional Ocean Modelling System (ROMS 3.4) and Incremental Strong-Constraint 4-Dimensional Variational (IS4D-Var) data assimilation. *Geosci. Model Dev.*, **9**, 3779–3801, https://doi.org/10.5194/gmd-9-3779-2016.

——, M. Roughan, and B. Powell, 2020: Predicting the submesoscale circulation inshore of the East Australian Current. *J. Mar. Syst.*, **204**, 103286, https://doi.org/10.1016/j.jmarsys.2019.103286.

Levin, J., H. G. Arango, B. Laughlin, J. Wilkin, and A. M. Moore, 2019: The impact of remote sensing observations on cross-shelf transport estimates from 4D-Var analyses of the Mid-Atlantic Bight. *Adv. Space Res.*, **68**, 553–570, https://doi.org/10.1016/j.asr.2019.09.01.

——, ——, ——, E. Hunter, J. Wilkin, and A. M. Moore, 2020: Observation impacts on the Mid-Atlantic Bight front and cross-shelf transport in 4D-Var ocean state estimates: Part I—Multiplatform analysis. *Ocean Modell.*, **156**, 101721, https://doi.org/10.1016/j.ocemod.2020.101721.

——, ——, ——, ——, ——, and ——, 2021: Observation impacts on the Mid-Atlantic Bight front and cross-shelf transport in 4D-Var ocean state estimates: Part II—The Pioneer Array. *Ocean Modell.*, **157**, 101731, https://doi.org/10.1016/j.ocemod.2020.101731.

Li, J., C. Kerry, and M. Roughan, 2021a: A high-resolution, 22-year, free-running, hydrodynamic simulation of the East Australia current system using the regional ocean modeling system (version 2.0). University of New South Wales, accessed 14 August 2021, https://doi.org/10.26190/TT1Q-NP46.

——, M. Roughan, and C. Kerry, 2021b: Dynamics of interannual eddy kinetic energy modulations in a western boundary current. *Geophys. Res. Lett.*, **48**, e2021GL094115, https://doi.org/10.1029/2021GL094115.

——, ——, and ——, 2022: Variability and drivers of ocean temperature extremes in a warming western boundary current. *J. Climate*, **35**, 1097–1111, https://doi.org/10.1175/JCLI-D-21-0622.1.

Macdonald, H. S., M. E. Baird, and J. H. Middleton, 2009: Effect of wind on continental shelf carbon fluxes off southeast

Australia: A numerical model. *J. Geophys. Res.*, **114**, C05016, https://doi.org/10.1029/2008JC004946.

Malan, N., B. Backeberg, A. Biastoch, J. V. Durgadoo, A. Samuelsen, C. Reason, and J. Hermes, 2018: Agulhas current meanders facilitate shelf-slope exchange on the Eastern Agulhas Bank. *J. Geophys. Res. Oceans*, **123**, 4762–4778, https://doi.org/10.1029/2017JC013602.

——, and Coauthors, 2020: Eddy-driven cross-shelf transport in the East Australian Current separation zone. *J. Geophys. Res. Oceans*, **125**, e2019JC015613, https://doi.org/10.1029/2019JC015613.

——, M. Roughan, and C. Kerry, 2021: The rate of coastal temperature rise adjacent to a warming western boundary current is nonuniform with latitude. *Geophys. Res. Lett.*, **48**, e2020GL090751, https://doi.org/10.1029/2020GL090751.

Mantovanelli, A., S. Keating, L. R. Wyatt, M. Roughan, and A. Schaeffer, 2017: Lagrangian and Eulerian characterization of two counter-rotating submesoscale eddies in a western boundary current. *J. Geophys. Res. Oceans*, **122**, 4902–4921, https://doi.org/10.1002/2016JC011968.

Mata, M. M., S. E. Wijffels, J. A. Church, and M. Tomczak, 2006: Eddy shedding and energy conversions in the East Australian Current. *J. Geophys. Res.*, **111**, C09034, https://doi.org/10.1029/2006JC003592.

Mellor, G. L., and T. Yamada, 1982: Development of a turbulence closure model for geophysical fluid problems. *Rev. Geophys.*, **20**, 851–875, https://doi.org/10.1029/RG020i004p00851.

Mertz, G., and D. G. Wright, 1992: Interpretations of the JEBAR term. *J. Phys. Oceanogr.*, **22**, 301–305, https://doi.org/10.1175/1520-0485(1992)022<0301:IOTJT>2.0.CO;2.

Morrison, A. K., A. M. Hogg, M. H. England, and P. Spence, 2020: Warm Circumpolar Deep Water transport toward Antarctica driven by local dense water export in canyons. *Sci. Adv.*, **6**, eaav2516, https://doi.org/10.1126/sciadv.aav2516.

Oke, P. R., and J. H. Middleton, 2000: Topographically induced upwelling off eastern Australia. *J. Phys. Oceanogr.*, **30**, 512–531, https://doi.org/10.1175/1520-0485(2000)030<0512:TIUOEA>2.0.CO;2.

——, G. B. Brassington, D. A. Griffin, and A. Schiller, 2008: The Bluelink ocean data assimilation system (BODAS). *Ocean Modell.*, **21**, 46–70, https://doi.org/10.1016/j.ocemod.2007.11.002.

——, and Coauthors, 2013: Towards a dynamically balanced eddy-resolving ocean reanalysis: BRAN3. *Ocean Modell.*, **67**, 52–70, https://doi.org/10.1016/j.ocemod.2013.03.008.

——, and Coauthors, 2019: Revisiting the circulation of the East Australian Current: Its path, separation, and eddy field. *Prog. Oceanogr.*, **176**, 102139, https://doi.org/10.1016/j.pocean.2019.102139.

Phillips, L. R., G. Carroll, I. Jonsen, R. Harcourt, and M. Roughan, 2020: A water mass classification approach to tracking variability in the East Australian Current. *Front. Mar. Sci.*, **7**, 365, https://doi.org/10.3389/fmars.2020.00365.

Pilo, G. S., R. O. Peter, T. Rykova, R. Coleman, and K. Ridgway, 2015: Do East Australian Current anticyclonic eddies leave the Tasman Sea? *J. Geophys. Res. Oceans*, **120**, 8099–8114, https://doi.org/10.1002/2015JC011026.

Ribbat, N., M. Roughan, B. Powell, S. Rao, and C. G. Kerry, 2020: Transport variability over the Hawkesbury Shelf (31.5–34.5°S) driven by the East Australian current. *PLOS ONE*, **15**, e0241622, https://doi.org/10.1371/journal.pone.0241622.

Ribbe, J., and D. Brieva, 2016: A western boundary current eddy characterisation study. *Estuarine Coastal Shelf Sci.*, **183**, 203–212, https://doi.org/10.1016/j.ecss.2016.10.036.

Rocha, C., C. A. Edwards, M. Roughan, P. Cetina-Heredia, and C. Kerry, 2019: A high resolution biogeochemical model (ROMS 3.4 + bio Fennel) of the East Australian Current system. *Geosci. Model Dev.*, **12**, 441–456, https://doi.org/10.5194/gmd-12-441-2019.

Rossi, V., A. Schaeffer, J. Wood, G. Galibert, B. Morris, J. Sudre, M. Roughan, and A. M. Waite, 2014: Seasonality of sporadic physical processes driving temperature and nutrient high-frequency variability in the coastal ocean off southeast Australia. *J. Geophys. Res. Oceans*, **119**, 445–460, https://doi.org/10.1002/2013JC009284.

Roughan, M., and J. H. Middleton, 2002: A comparison of observed upwelling mechanisms off the east coast of Australia. *Cont. Shelf Res.*, **22**, 2551–2572, https://doi.org/10.1016/S0278-4343(02)00101-2.

——, and ——, 2004: On the East Australian current: Variability, encroachment, and upwelling. *J. Geophys. Res.*, **109**, C07003, https://doi.org/10.1029/2003JC001833.

——, P. R. Oke, and J. H. Middleton, 2003: A modeling study of the climatological current field and the trajectories of upwelled particles in the East Australian current. *J. Phys. Oceanogr.*, **33**, 2551–2564, https://doi.org/10.1175/1520-0485(2003)033<2551:AMSOTC>2.0.CO;2.

——, H. S. Macdonald, M. E. Baird, and T. M. Glasby, 2011: Modelling coastal connectivity in a Western Boundary Current: Seasonal and inter-annual variability. *Deep-Sea Res. II*, **58**, 628–644, https://doi.org/10.1016/j.dsr2.2010.06.004.

——, S. R. Keating, A. Schaeffer, P. Cetina-Heredia, C. Rocha, D. Griffin, R. Robertson, and I. M. Suthers, 2017: A tale of two eddies: The biophysical characteristics of two contrasting cyclonic eddies in the East Australia Current System. *J. Geophys. Res. Oceans*, **122**, 2494–2518, https://doi.org/10.1002/2016JC012241.

Sarkisyan, S., and V. Ivanov, 1971: Joint effect of baroclinicity and bottom relief as an important factor in the dynamics of the sea current. *Izv. Acad. Sci. USSR*, **7**, 173–188.

Schaeffer, A., and M. Roughan, 2017: Subsurface intensification of marine heatwaves off southeastern Australia: The role of stratification and local winds. *Geophys. Res. Lett.*, **44**, 5025–5033, https://doi.org/10.1002/2017GL073714.

——, ——, and B. D. Morris, 2013: Cross-shelf dynamics in a Western Boundary Current regime: Implications for upwelling. *J. Phys. Oceanogr.*, **43**, 1042–1059, https://doi.org/10.1175/JPO-D-12-0177.1.

——, ——, and J. E. Wood, 2014: Observed bottom boundary layer transport and uplift on the continental shelf adjacent to a western boundary current. *J. Geophys. Res. Oceans*, **119**, 4922–4939, https://doi.org/10.1002/2013JC009735.

Schilling, H. T., J. D. Everett, J. A. Smith, J. Stewart, J. M. Hughes, M. Roughan, C. Kerry, and I. M. Suthers, 2020: Multiple spawning events promote increased larval dispersal of a predatory fish in a western boundary current. *Fish. Oceanogr.*, **29**, 309–323, https://doi.org/10.1111/fog.12473.

Spence, P., R. M. Holmes, A. M. Hogg, S. M. Griffies, K. D. Stewart, and M. H. England, 2017: Localized rapid warming of West Antarctic subsurface waters by remote winds. *Nat. Climate Change*, **7**, 595–603, https://doi.org/10.1038/nclimate3335.

Su, C. H., and Coauthors, 2019: BARRA v1.0: The Bureau of Meteorology Atmospheric high resolution Regional Reanalysis for Australia. *Geosci. Model Dev.*, **12**, 2049–2068, https://doi.org/10.5194/gmd-12-2049-2019.

Vélez-Belchí, P., L. R. Centurioni, D. K. Lee, S. Jan, and P. P. Niiler, 2013: Eddy induced Kuroshio intrusions onto the continental shelf of the East China Sea. *J. Mar. Res.*, **71**, 83–107, https://doi.org/10.1357/002224013807343470.

Webb, D. J., R. M. Holmes, P. Spence, and M. H. England, 2019: Barotropic Kelvin wave-induced bottom boundary layer warming along the West Antarctic Peninsula. *J. Geophys. Res. Oceans*, **124**, 1595–1615, https://doi.org/10.1029/2018JC014227.

Whiteway, T. G., 2009: Australian bathymetry and topography grid, June 2009. Australian Government Geoscience Australia, accessed 23 January 2021, https://data.gov.au/data/dataset/australian-bathymetry-and-topography-grid-june-2009.

Wood, J. E., M. Roughan, and P. M. Tate, 2012: Finding a proxy for wind stress over the coastal ocean. *Mar. Freshwater Res.*, **63**, 528–544, https://doi.org/10.1071/MF11250.

Zaba, K. D., D. L. Rudnick, B. D. Cornuelle, G. Gopalakrishnan, and M. R. Mazloff, 2020: Volume and heat budgets in the coastal California Current System: Means, annual cycles and interannual anomalies of 2014-2016. *J. Phys. Oceanogr.*, **50**, 1435–1453, https://doi.org/10.1175/JPO-D-19-0271.1.

Zhang, W. G., and G. G. Gawarkiewicz, 2015: Dynamics of the direct intrusion of Gulf Stream ring water onto the Mid-Atlantic Bight shelf. *Geophys. Res. Lett.*, **42**, 7687–7695, https://doi.org/10.1002/2015GL065530.

——, and J. Partida, 2018: Frontal subduction of the Mid-Atlantic Bight shelf water at the onshore edge of a warm-core ring. *J. Geophys. Res. Oceans*, **123**, 7795–7818, https://doi.org/10.1029/2018JC013794.